ABSTRACT

Title of Document:	DEVELOPMENT OF AN ADAPTIVE MASKING METHOD TO IMAGE BEAM HALO
	Hao Zhang, Master of Science, 2011
Directed By:	Professor Patrick G. O'Shea Department of Electrical and Computer Engineering Dr. Ralph B. Fiorito and Professor Rami A. Kishek Institute for Research in Electronics and Applied Physics

Beam halo is a common phenomenon in most intense particle beams and is associate with many bad effects. Halo is very hard to characterize because of its low intensity, which requires a measurement system with high dynamic range ($\geq 10^5$). Here, we have developed a technique that employs a digital micro-mirror array to produce an image of the halo of an electron beam with an enhanced dynamic range. Light produced by the beam intercepting a phosphor screen is first imaged onto the array; an adaptive mask is created and applied to filter out the beam core; and the result is reimaged onto an CCD camera. In this thesis, we describe the optics used, the masking operation and preliminary results of experiments we have performed to study beam halo at the University of Maryland Electron Ring.

DEVELOPMENT OF AN ADAPTIVE MASKING METHOD TO IMAGE BEAM
HALO

By

Hao Zhang

Thesis submitted to the Faculty of the Graduate School of the
University of Maryland, College Park, in partial fulfillment
of the requirements for the degree of
Master of Science
2011

Advisory Committee:
Professor Patrick G. O'Shea, Chair
Dr. Ralph B. Fiorito, Co-chair
Professor Rami A. Kishek
Professor Victor L. Granatstein

Dedication

To my parents, Lang Zhang and Furong Tang

Acknowledgements

I would like to thank Professor Patrick O'Shea first for the financial support for this study. His insight of this field and fruitful guidance inspired me during the time of this thesis. I would like to thank Dr. Ralph Fiorito, who contributed great on this work. He helped me with his thoughtful suggestion and tremendous efforts on my thesis work from the beginning to the end. I would like also to give thanks to Professor Rami A. Kishek for his direct assistance and patience in the revision of this thesis. Particularly, I would like to thank Dr. Anatoly Shkvarunets for his generosity to offer an optics code and give meaningful suggestion on the optics design. In addition, I would like to thank Professor Victor Granatstein for serving on my defense committee.

Table of Contents

List of Tables

List of Figures

Chapter 1: Introduction

1.1 General background

Particle accelerator physics and technology is a developing branch in science. Many particle accelerators have been built and applied to research fields as well as industry and manufacturing. For most of the well-known accelerators, such as the Tevatron [1], the Stanford Linear Collider (SLC) [2], the Large Hadron Collider (LHC) [3], and so on, their goals were to create high energy particles and provide essential tool for the study of nuclear and particle physics. In addition, other accelerators, covering a wide range of beam energies, sizes and currents, are designed for light sources [4, 5], free electron lasers [6-8], spallation neutron sources [9], potential driver for ion fusion [10] and so on. For these applications, high energy beams are not the only goal, but high current and intense beams are required, which means that the accelerators should transport and accelerate as many charged particles as possible while keeping a good beam quality. In beam physics, beam quality is often characterized by emittance (proportional to phase space volume of beam), but dynamically depends on the detail knowledge of phase space.

Here, as beam current increases, the space charge force will play an important or even dominant role in the particle dynamics and affect the beam size and particle trajectory [11]. It can also be highly nonlinear, leading to many exotic phenomenons, one of which is beam halo, the subject of this thesis.

1.2 Beam halo and previous theoretical studies

In beam physics, halo is a population of particles that travel to large radii away from most particles of the beam (called the "core"). So far, there is no well-accepted, rigorous definition of halo, but it has been observed in many intense beams [12, 13], and in the injection part of many high energy accelerators [14, 15]. Beam halo is associated with emittance growth and thus decreases beam quality. More seriously, some halo particles in large radius will hit the beam pipe and be lost. For high energy beam, the lost particles contribute to the nuclear activation of wall material and cause potential health issues for the accelerator workers and thus increase maintenance expense. For positively charged beams, the secondary electron emission from the impact of halo particles can result in electron cloud around the beam and make the dynamics more complicated. Although large beam pipe can be used to accommodate the halo, the cost of larger magnets, radio frequency cavities and etc. will grow significantly.

Previous theoretical studies proposed several mechanisms for halo formation. As indicated in particle-core model [16], Gluckstern indicated how parameter resonance can drive particles out of beam core to large amplitudes, forming a distribution of halo. Wangler [17], from particle-core simulations, proved the maximum amplitude of halo distribution depends on the magnitude of the mismatch parameter (for example initial beam radius in [17]), again in the framework of particle-core model. Qiang [18] extended this model to a 3D mismatched anisotropic beam and Ikegami [19] discussed the model in a periodic focusing channel. Kishek [20] pointed out that the beam halo can also arise from skew mismatches, for

example, caused by quadrupole rotation errors. Papadopoulos [21] simulated the regeneration of phase space halo after removal of halo in real space. Despite the wealth of theoretical and simulation studies, the mechanism of beam halo formation is not yet fully understood, and experimental studies have been few.

1.3 Previous Experimental Studies

The biggest challenge in measuring beam halo is the dynamic range of the diagnostics [22]. The particle loss specification of many accelerators, for example SNS, can be quite stringent (e.g. one in 10^6 particle per meter). Meaningful measurements need to therefore cover a dynamic range of at least $10^5 \sim 10^6$ in order to detect faint halos. There are several methods being used or having the potential to measure beam halo, such as (a) wire-scanner, (b) Ionization beam profile monitor, and (c) beam imaging including the Saturated-core method and spatial filtering method.

Wire scanners [23] measure the beam profile directly and are used in many accelerators. Recently, at the Low Energy Demonstration Accelerator (LEDA) in Los Alamos National Laboratory, researchers [24, 25] use a wire scanner and halo scraper combination. The wire scanner is used to measure the core of the distribution and water-cooled graphite scraping device to measure the tail of the distribution as shown in Fig 1.2. In the experiment, they demonstrated a dynamic range of more than 10^5:1, and provide distribution information to $5 \sim 7$ times typical RMS widths of the beam. This method can give 1D spatial information of beam at one time, but the disadvantage is that the measurement is slow and large current may burn the wires.
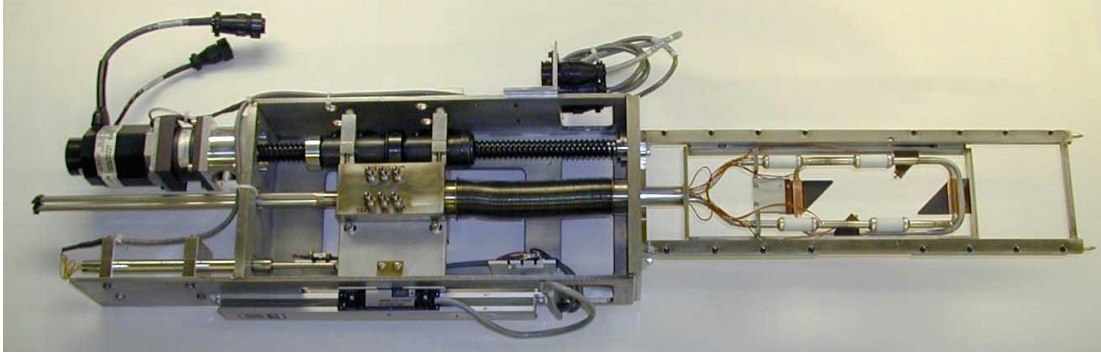
Figure 1.1: Halo Scraper/Wire Scanner Assembly [25].

The Ionization beam profile monitor (IPM) [26] illustrate in Fig.1.2 measures the ionization signal induced by the beam electrons as they pass through the residual gas in the beam line. This method collects and measures the secondary electron generated in the residual gas using a micro-channel plate amplifier and data collection circuit board. Most references report that the dynamic range of this method does not exceed 10^3. However, after further modification and improvement, the IPM, explained by Connolly, et al [27], can be a potential beam halo monitor.
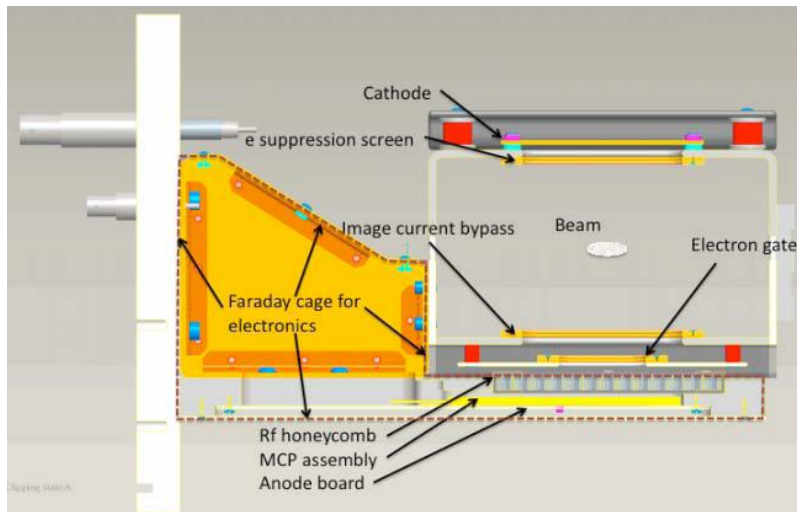
Figure 1.2: Layout of the IPM [27]

High dynamic range beam imaging is also useful to measure beam halo. We list two approaches here in detail, one of which is the saturated-core method. The

principle of the saturated-core method [28], as indicated by its name, is to change the light amplification of an intensified CCD (charge-coupled device) camera to measure beam core below saturation, while measuring the halo with beam core saturated. One drawback of this method is the possible spoilage of the halo observation because of some unwanted phenomenon such as contamination from beam core and blooming in the CCD pixels. Moreover, the CCD can be damaged by large saturation. To avoid the saturation, a Spectra-Cam CID (charge injection device) camera with a high dynamic range was suggested [29]. The key feature of CID camera is that, when the pixels reach to the maximum, they will return to their original bias conditions allowing for the continued integration without saturation. Welsch and et al [29] demonstrated a dynamic range of 10^5 by measuring a laser profile with a neutral density filter. The disadvantage of the CID camera is the expensive price.

The spatial filtering method can avoid the damage caused by core saturation. One example of this method is OTR (optical transition radiation) screen with a hole in the center [28]. By steering the beam core right through the hole in the center of the OTR screen, the distribution of halo particles can be observed. Another case is coronagraph principle applied to beam halo imaging [29, 30]. An optical system using this method is shown in Fig. 1.3. In the figure, a light blocking spot mask is printed on polyesther foil is used to filter the central area of the beam image which is projected on the foil. The remainder of the beam image is then re-projected onto a camera. Moreover, by introducing a Lyot stop to remove the diffraction effects of objective lenses and the opaque blocking disk, as shown in Fig. 1.4, Mitsuhashi [30] was able to attain a higher contrast between beam and halo, and demonstrated a

5

dynamic range over 10^6. For a regular or fixed shape of beam core, these two spatial filtering methods work very well, and a high dynamic range can be also achieved. However, if the beam core varies, the shape of the screen hole or filtering spot on the foil needs to be changed likewise, which makes it hard to implement.
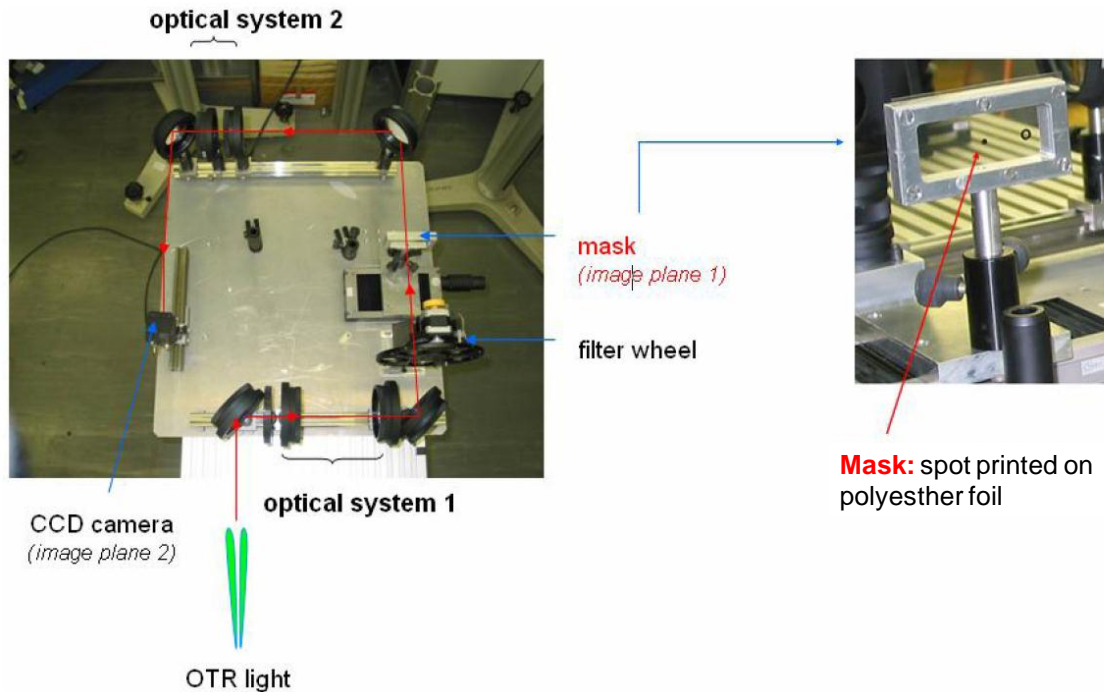
Figure 1.3: Experimental setup for coronagraph method applied in halo measurement [29].
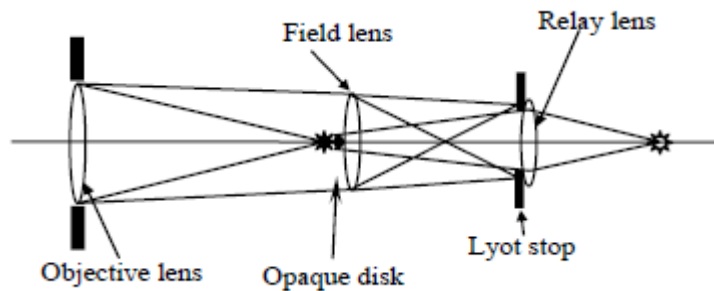
Figure 1.4: Layout of coronagraphy method with Lyot stop [30].

6

1.4 Imaging method using digital micro-mirror-array device (DMD)

In this thesis, we will talk about a new imaging method using a digital micro-mirror-array device (DMD). When incorporated into an imaging system, the device can be used as a spatial light modulator. This method is similar to the spatial filtering or masking method, but with the advantage that the shape of the mask can be adaptively modified to conform to the shape of the beam. The DMD is a digitally controlled MEMS device widely used in the commercial imaging products such as HDTV and projectors under the commercial name DLP (Digital Light Processor). In our experiment, we use the DMD Discovery 1100 manufactured by Texas Instruments Inc. [31] as shown in Fig. 1.5 (a).

(a)

13.68 um

(b)

12⁰

(c)
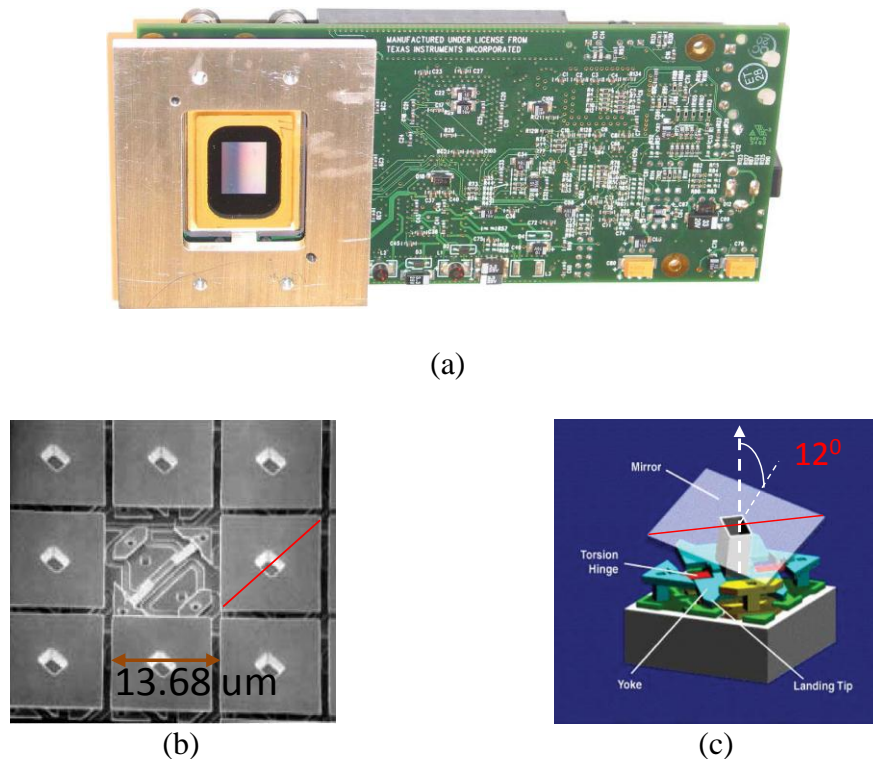
Figure 1.5: (a) Digital mirror-array device; (b) segment of the DMD [31]; (c) mechanical drawing of individual micro-mirror and substructure [31].

The device contains a digital micro-mirror array chip as well as a controller board. There are 1024 × 768 pixels on the chip, each of which has a micro-mirror on the surface. Figs. 1.5 (b) and (c) show an enlarged segment of the mirror array and a mechanical drawing of one pixel, separately. As illustrated on Fig. 1.5 (c), each pixel contain a 13.68 μm ×13.68 μm aluminized silicon micro-mirror which can be individually addressed electronically and rotated about the diagonal line ±12°, to an 'on' or 'off' state, when a positive or negative voltage is applied to electrodes underneath its corners. When the voltage to the DMD is zero, all the micro-mirrors are in a nominally flat, floating state. In the 'on' state, the incident light is reflected towards the camera. Otherwise, in the 'off' state, the light will directed 48° away from that optical path. Some important features of the device are listed in Table 1.1.

Table 1.1 DMD Discovery 1100 key features [31]

Parameter	Value
Chip size	14.3 mm × 10.8 mm
Mirror size	13.68 μm ×13.68 μm
Resolution	1024 × 768 pixels
Switching rate	9,600 frames/s
PC interface	USB 2.0
Control	GUI, also allow ActiveX control

The optical filtering ability of DMD has been demonstrated, and it was used to measure the profile of a laser [32] as illustrated in Fig. 1.6. Only the spatial distribution of the core of laser can be measured without masking out the core, because of the high contrast between core and the tails. However, by using the DMD

to generate a core blocking mask, the light from the laser beam core is reflected to another direction, so that the rest of the profile can be measured. As indicated in Fig. 1.7, Egberts [32] showed the DMD in combination with an 8-bit CCD camera could be used to make a laser profile measurement with a dynamic range of 10^5.

(a) Laser profile measurement   (b) Display beam core on DMD
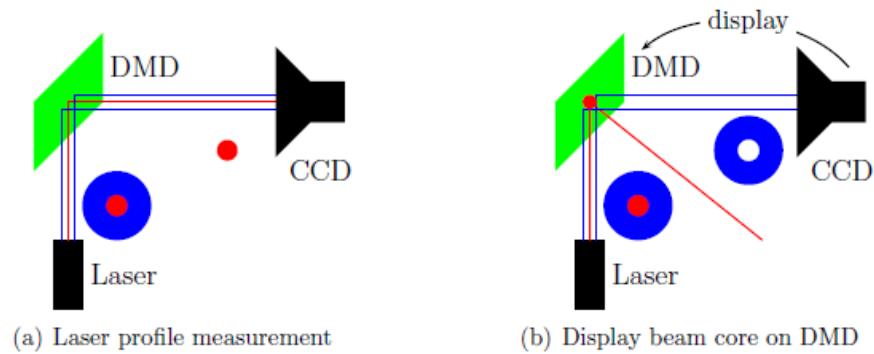
Figure 1.6: Laser profile measurement using DMD [32].
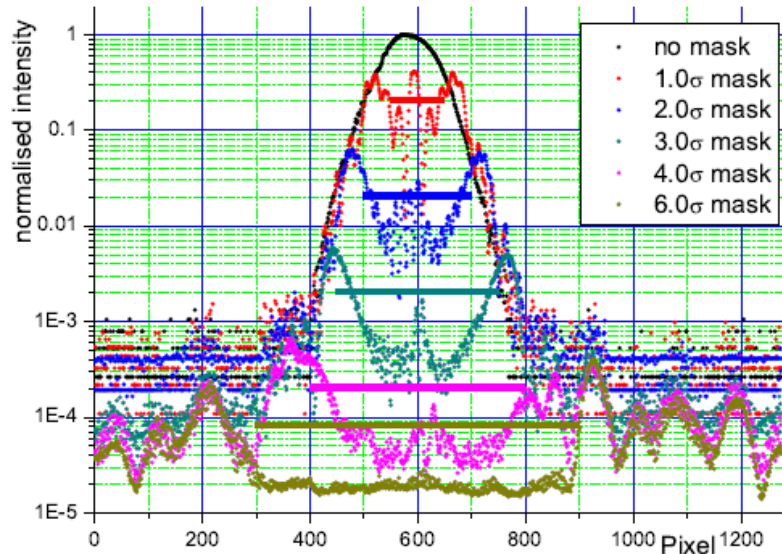
Figure 1.7: Laser images with various mask sizes with horizontal bars to indicate the mask size [32].

Egberts also showed that, the mask generated on the DMD used to block out the light from the high intensity laser core can be changed adaptively, conforming to the core shape. This makes the spatial filtering method more useful and practical in a

9

beam imaging system. In this thesis, I present the first application of this technique to image a particle beam with a halo. I tested the method using the University of Maryland Electron Ring (UMER) [33], and demonstrated its effectiveness.

1.5 Organization of this thesis

In Chapter 2, we will illustrate the concept of using DMD in the optical system and give detailed information about the benchmark optics. After that, I describe the optical systems developed for benchmark testing and beam imaging, as well as the mask generation algorithm. The whole chapter will concentrate on how this method works. In Chapter 3, I present resent results using this method including performance tests of the optical imaging system and the results of first beam halo measurement. In Chapter 4, we summarize the results and suggest future applications and experiments.

Chapter 2: Experimental Setup

In this chapter, we will first explain the concept for optical imaging system using digital micro-mirror-array device (DMD). This is followed by the discussion of the layout design on the bench. Some of the peculiar features of the DMD need to be addressed in order to easily incorporate the DMD into the design. After that, we apply this benchmark optical design to an experimental setup to image a real beam, in particular, one produced by the University of Maryland Electron Ring (UMER).

2.1 Experimental concept
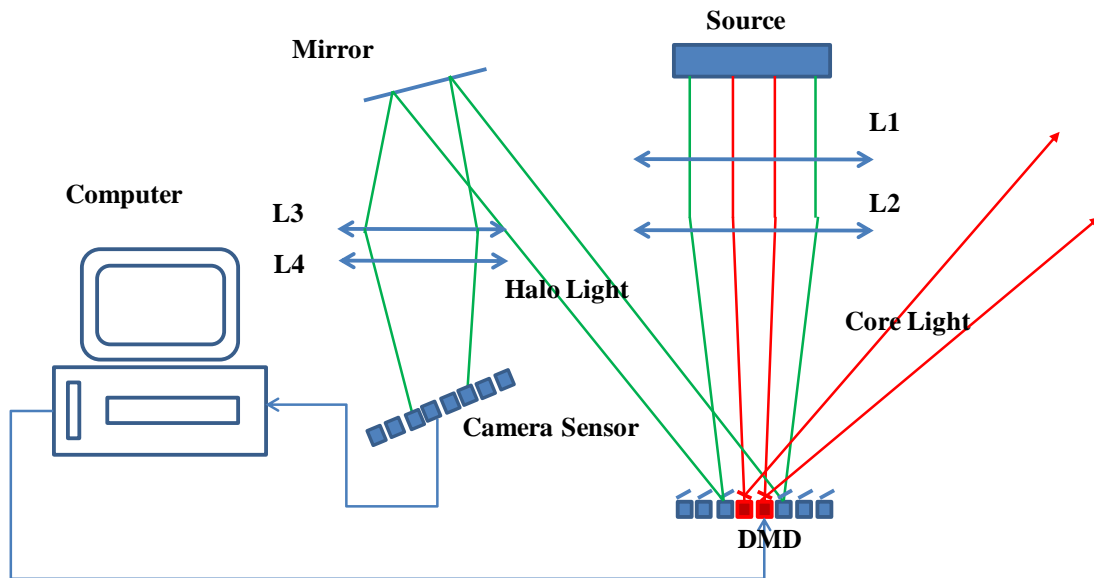
Figure 2.1 Schematic layout of halo experimental concept using DMD

A schematic of our optical design is shown in Fig. 2.1. Here the source can be the beam image produced by an interceptive source, e.g. phosphor, YAG (Yttrium aluminum garnet) or OTR (optical transition radiation), or a non-intercepted source, e.g. optical synchrotron, edge or undulator radiation. We first optically transport the source image onto the DMD by using two lenses L1 and L2 to control both the

magnification and focusing. Then we reimage the image formed on the DMD to the camera sensor using two additional lenses L3 and L4, which control the size and focus of the final image on the CCD sensor. After we obtain the picture of beam and identity the intensity level of core which we wish to reject, we program the DMD to generate a mask, which filters out the higher intensity beam core, as represented by the red rays in Fig. 2.1. The filtered image is retaken by integrating over an increased number of frames (or pulses) to achieve an image of the halo using the full dynamic range of the CCD sensor. Consequently, this method enhances the dynamic range of the whole measurement.

2.2 Benchmark test using DMD
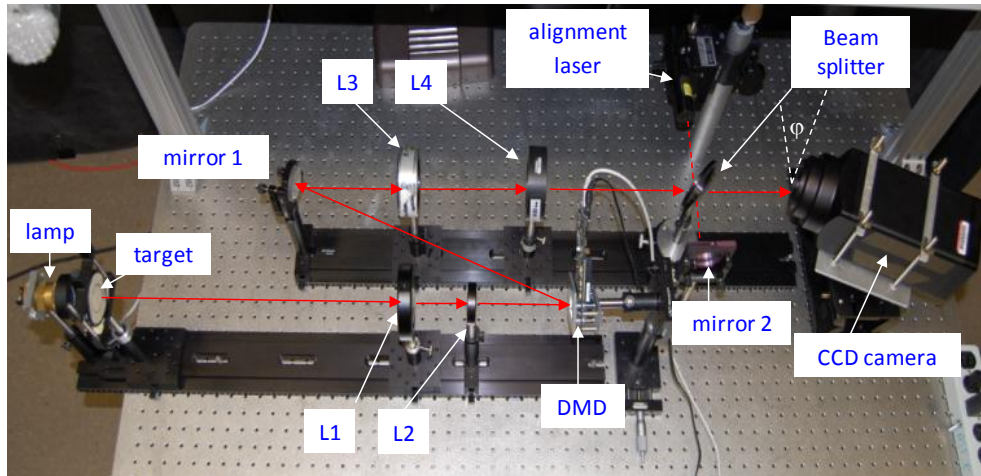
Figure 2.2: Picture of benchmark test for DMD and optical design

Fig. 2.2 shows the picture of the optics used for our benchmark tests. The purpose of this setup is to develop a simple optical system which simulates the optical features of the real source (e.g. a phosphor screen used in UMER to image the beam) and which can be easily adapted to image the beam halo in other accelerators. A back-lighted circular target is used which has a rectangular grids and is 32 mm in

diameter. It has almost the same dimension as the phosphor screen (31.75 mm) used in UMER. From Fig. 2.2, the source (target), lenses L1, L2 and the DMD are considered to be one of the two optical channels. The second channel contains the DMD, lenses L3, L4 and the CCD system. The CCD we use is the PIMAX2 manufactured by Princeton Instruments, which features a 512×512 pixels, 16 bits, cooled CCD sensor with an intensifier which can be gated as short as 3 ns. The transverse size of the intensifier is 15.8 mm × 15.8 mm. It contains a photocathode, micro-channel plate (MCP) and fluorescent screen. In the intensifier, the light from the image hit the photocathode and generate the electrons. The number of electrons will be amplified in the MCP. Then, the electrons hit the florescent screen to re-obtain a intensified image. This image on the florescent screen of the intensifier will reduce to the size of CCD (12.4 mm × 12.4 mm) by a fiber-optic bundle which connects the CCD and the intensifier.

Later in this chapter, when we talk about the size of the CCD sensor in order to calculate the magnification, we mean the size of intensifier. Notice that we use the CCD camera without a directly coupled lens because we need to tilt the camera for compensation which will be discussed later. If a directly coupled lens is used for the CCD camera, it will also be tilted which will decrease the acceptant angle of the CCD sensor and even block the light pathway.

The alignment procedure for the optics is presented in Appendix A.

2.2.1 Optical channel I

In the first optics channel, we want to transport the target image to DMD as shown in Fig. 2.3. Here, each micro-mirror is normal to the axis, when the device is

in the floating state (the power of the DMD is off). In order to get the best spatial filtering resolution with the DMD, we require that the image of the entire target (32 mm in diameter) fills the DMD (14.3 mm × 10.8 mm in size), with the diameter of the target image extending to the shortest size of the DMD. Thus, the required magnification for the first optical channel is 10.8 mm / 32 mm = 0.338. Using this magnification and the total distance between the target and the DMD (737 mm as shown in Fig. 2.3), substituted into Eqn. 2.1

$$f_{eff} = \frac{m*d}{(m+1)^2}$$

(2.1)

where d is total distance between object and image, and m is the magnification defined by the ratio of image size and object size, we can calculate the focal length of the effective lens as 140 mm. In practice, we choose readily available lenses, L1 (320 mm) and L2 (200 mm), and manually adjust them to achieve the correct magnification and focus of the target onto the surface of the DMD.
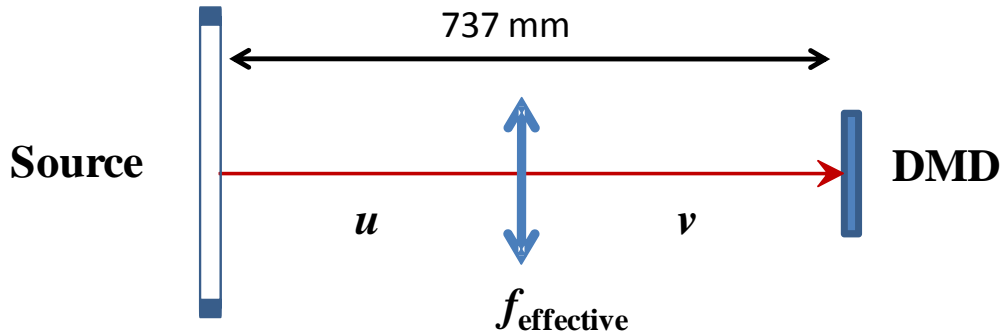
Figure 2.3: Schematic of the first optical channel

As mentioned in section 1.3, the rotation axis of each micro-mirror is along the diagonal. Thus, if the DMD is positioned so that its vertical axis is normal to the ground, after DMD powering, the micro-mirrors on the chip will reflect the incident light out of the horizontal plane. In order to compensate for this, we rotate the DMD

45 ° to make the rotation axis of each micro-mirror correspond to the vertical as seen in Fig. 2.4 (a). As a result, no matter how the micro-mirrors flip, the light pathway is maintained in the horizontal plane. This means that the center of all the optical components can be set in the same plane. This greatly simplifies the positioning and the alignment of all the optical components in both channels.

(a)   (b)
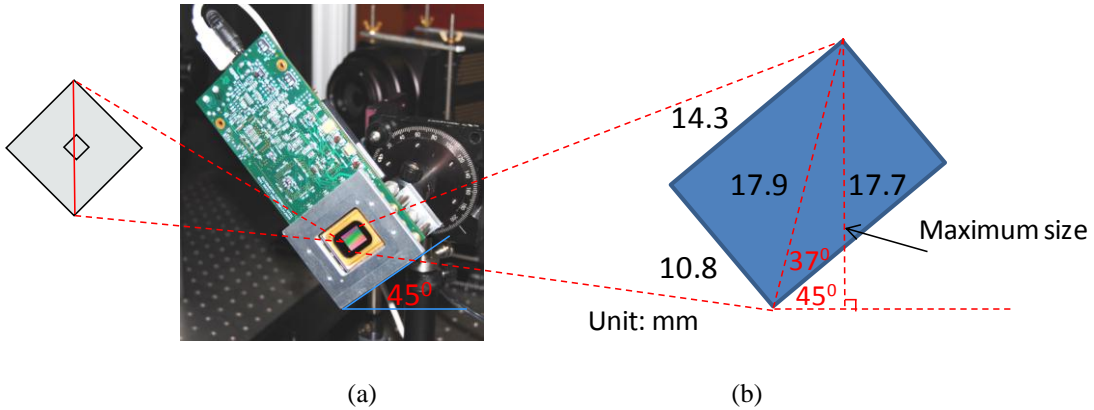
Figure 2.4: Picture of rotated DMD in the optical system and enlarged sketch of micro-mirror (a) and enlarged sketch of DMD chip(b)

2.2.2 Optical channel II
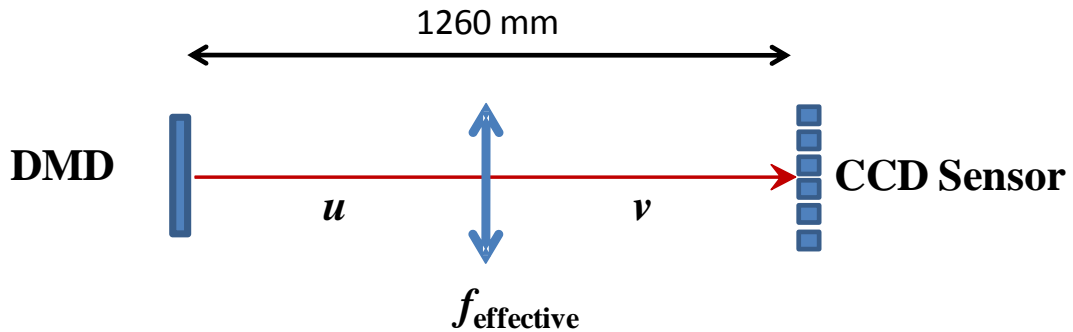
Figure 2.5: Schematic of second optical channel

When we switch all the micro-mirrors to the "on" state (+12 °), the image of the target focused on the DMD by the first channel is now directed into the second optical channel as shown in Fig. 2.5. In order to get the best spatial resolution on the CCD, we require that the image of the entire DMD (14.3 mm × 10.8 mm in size) fills

the CCD sensor (15.8 mm × 15.8 mm, size of the intensifier). Notice that, since the DMD is tilted 45 ° with respect to the vertical axis, 17.7 mm is maximum size which fills the CCD sensor (see Fig. 2.4 (b)). Then the required magnification is 15.8 mm / 17.7 mm = 0.892. This magnification together with the distance between the DMD and the CCD sensor (1260 mm) determines the focal length of the effective lens for the second optical channel, which is 314 mm (see Eqn. 2.1). Readily available lenses, L3 (860 mm) and L4 (420 mm), are used to produce this effective focal length.
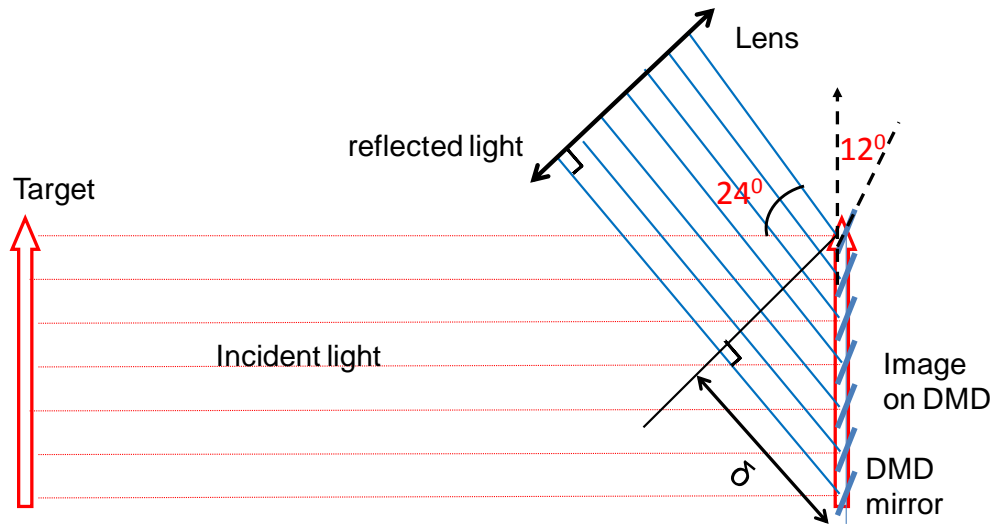
Figure 2.6: Path length difference generated by DMD tilted mirror

As indicated in Fig. 2.6, the DMD plane is not parallel to the lens plane. If we position the camera sensor normal to the optical axis, we will obtain an image with distortion and a non-uniform focus in the horizontal direction. This is due to the +12 ° tilt angle of the micro-mirrors, which produces differences in the path lengths of the rays (see δ in fig. 2.6) emanated from different horizontal source points on the DMD. As a result, the plane of the image that is produced by lenses L1 and L2 on the DMD is not parallel to the plane of lens L3 or L4. To compensate for this, the CCD sensor

16

must be rotated by an angle φ with respect to the vertical (see Fig. 2.2). This method is commonly used in photography and is known as Scheimpflug compensation [35]. Fig. 2.7 shows how it works.

For the second optical channel (see Fig. 2.7), the plane of the image on the DMD is not parallel to the lens plane, but has an angle $\theta = 24°$, which is exactly twice the flipped angle (12°) for each micro-mirror. According to the Scheimpflug principle, the plane of camera sensor must be rotated by an angle φ, in order to achieve focusing of this inclined source onto the CCD sensor. This angle is determined by Eqn. 2.2 (see Appendix B for the derivation),

$$\varphi = \arctan(\frac{m+1}{m}\tan\theta) - \theta \tag{2.2}$$

where θ is titled angle of DMD according to the lens plane which in our case is always 24°, and m is the magnification of the second channel of the imaging system.
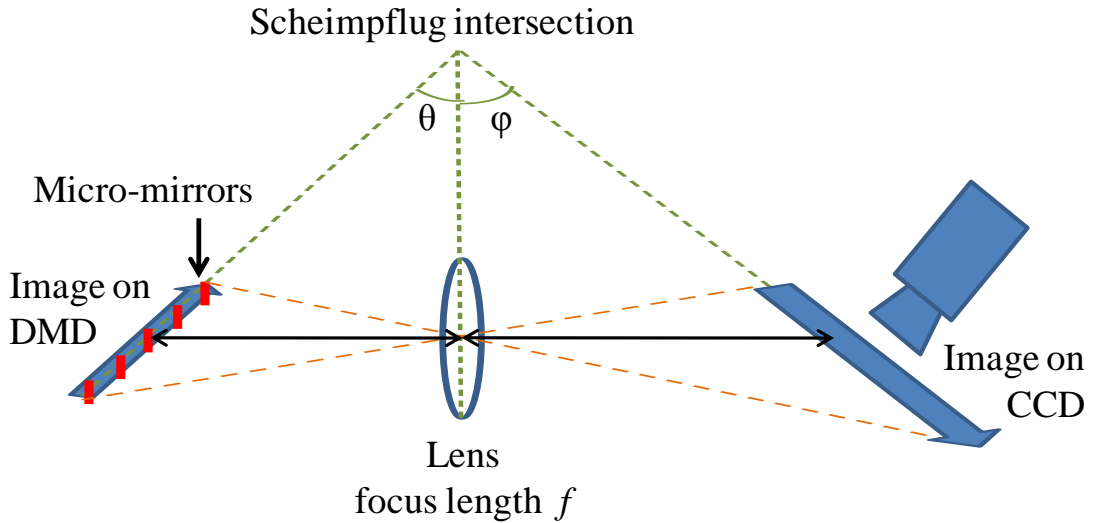
Figure 2.7: Compensation by rotating camera based on Scheimpflug principle

Note that, in Appendix B, m equal to the ratio of image-to-lens distance and object-to-lens distance which does not generally equal to the magnification calculated

by the ratio between image size and object size as we do in this sub section, but the latter is still a good approximation to guide us to empirically find the sheimpflag angle for CCD sensor. Fig. 2.8 gives the final location of each optical component. After substituting the magnification (0.892) of the second channel into the formula, we find the sheimpflag angle for CCD sensor is 19.4 °.
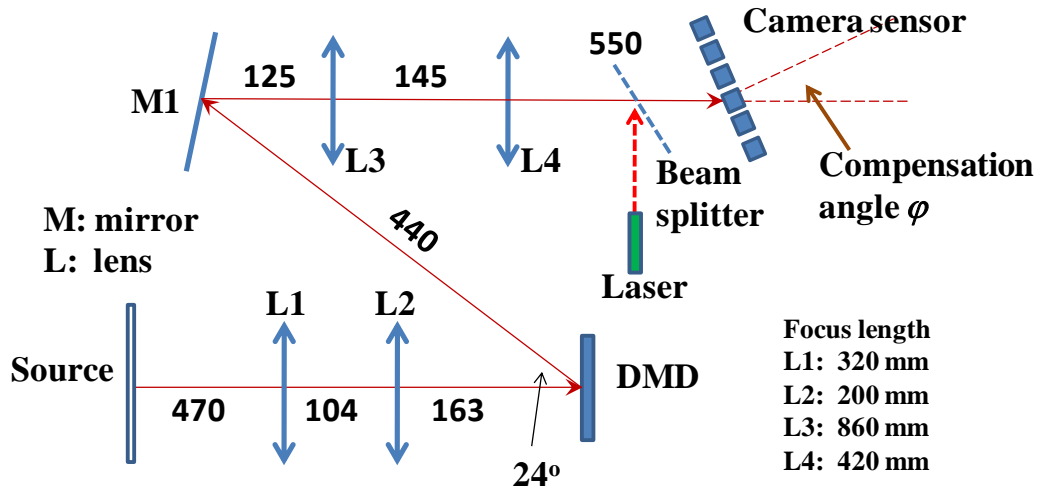
Figure 2.8: The benchmark layout with location of each component

In practice, we do the compensation empirically by adjusting the angle of rotation of the PIMAX2 camera so as to allow the image of the target on the CCD to be equally focused on both horizontal sides, and minimally distorted, i.e. by observing the horizontal and vertical sized of the rectangular grid cells). When we swing the camera, we also transit the camera horizontally to keep the image in the center. Because of errors in distance measurement and the approximation we made for the magnification, the calculated value of the compensation angle φ is not the same as the one measured which about 24 °. Fig. 2.9 shows a picture of target as well as the tilted DMD chip with the Scheimpflug compensation. We can see that, 1) the target circle fills the DMD chip; 2) the DMD chip almost fills the CCD sensor; 3) by

18

rotating the sensor by the compensation angle, we obtain a well focused (across the horizontal) and undistorted image .
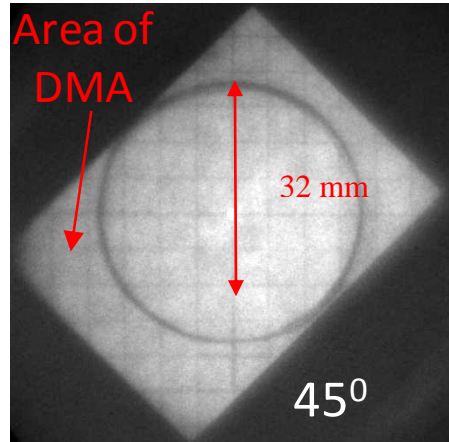
Figure 2.9: Image of the test target on the CCD with Scheimflug compensation

2.3 Experimental setup in UMER

For a proof-of-principle test of the DMD masking method for halo imaging described above, we use the University of Maryland Electron Ring (UMER) to generate the electron beam with and without halo.

2.3.1 University of Maryland Electron Ring (UMER)

UMER [35] is a scaled machine, using 10 keV electrons at relatively high currents (~1-100 mA), to access space charge physics. UMER is well-suited for this experiment since (a) it can generate beam with and without halos easily; (b) screen works well for a lot of light. Fig. 2.10 shows a schematic of the UMER layout, while Table 2.1 lists key parameters.
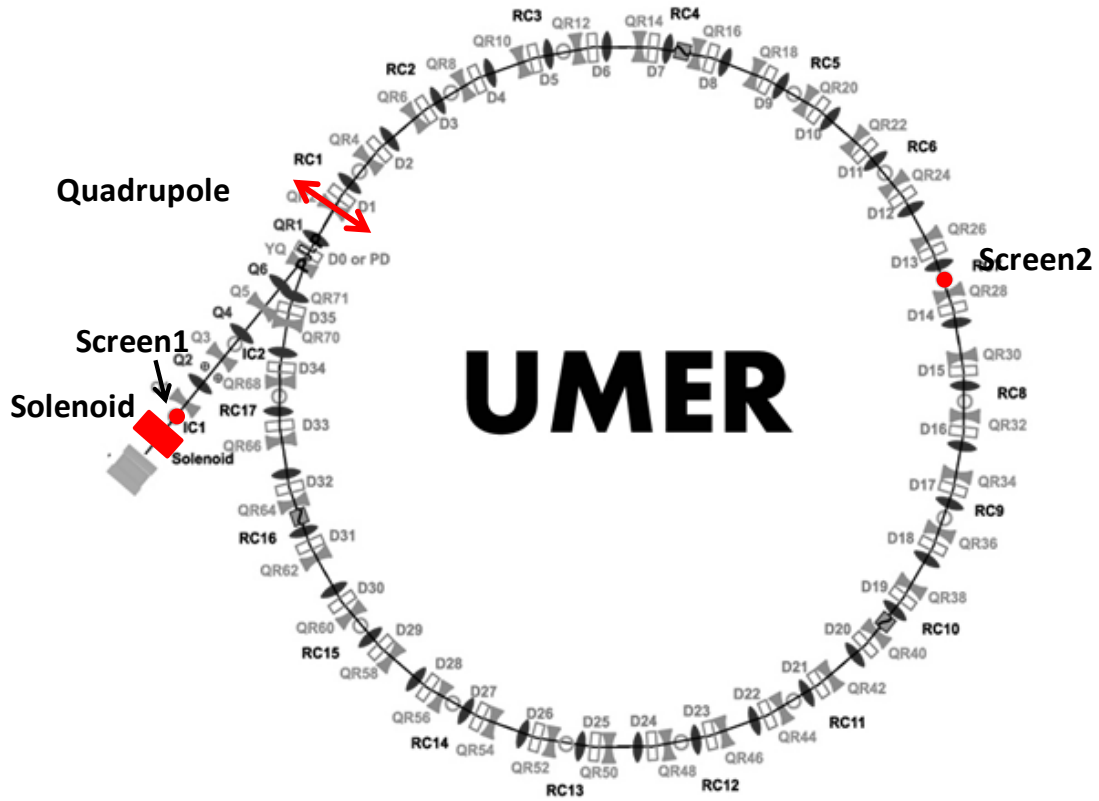
Figure 2.10: Schematic layout of UMER

Table 2.1: UMER design parameters [35]

Beam Energy	10 keV
$\beta = v/c$	0.2
Pulse Length	20-120 ns
Current	0.5-100 mA
Ring Circumference	11.52 m
Lap Time	197 ns
Pulse Repetition Rate	10-60 Hz
FODO Period	0.32 m
Zero-current Phase Advance	0.760

In addition, UMER beams are pulsed at certain repetition rate from 10 - 60 Hz, and they are reproducible over many pulses, allowing us to do frame integration with minimum error due to shot-to shot variation.

Furthermore, as listed in Table 2.2, a key feature of UMER is the ability to vary the beam intensity. The related intensity parameter χ, the ratio between space charge force and external focusing force, can be varied from emittance domain region to intense space charge domain region, by applying different apertures and thus changing the beam currents. An aperture wheel with several apertures is located right after the electron gun exit to do this variation. The different intensity level allow us to study different forming halo formation mechanisms, including magnet alignment, mismatch, resonance, space charge and so on.

Table 2.2: Beams in UMER [36]

Aperture#	r_0 （mm）	I (mA)	ε (μm)	χ
1	0.25	0.6	7.6	0.27
2	0.875	6	25.5	0.6
3	1.5	21	39.0	0.32
4	2.85	78	86.6	0.84
5	3.2	104	97.3	0.90

As shown in Fig. 2.10 highlighted with red, we collect data at two diagnostic chambers: 1) IC1 in the injection line, where the beam core is round. We can adjust the bias voltage in the gun as well as the solenoid to perturb the beam for test; 2) RC7 in the ring, where the beam distribution is more complex. By varying the quadrupole upstream, for example QR2, we can mismatch the beam and generate halo.

2.3.2 Optical design at UMER

We apply the benchmark optics into our real experiment. Fig.2.11 shows a picture of the experiment setup in IC1. Fig. 2.12 shows a layout of the experiment setup also in IC1.
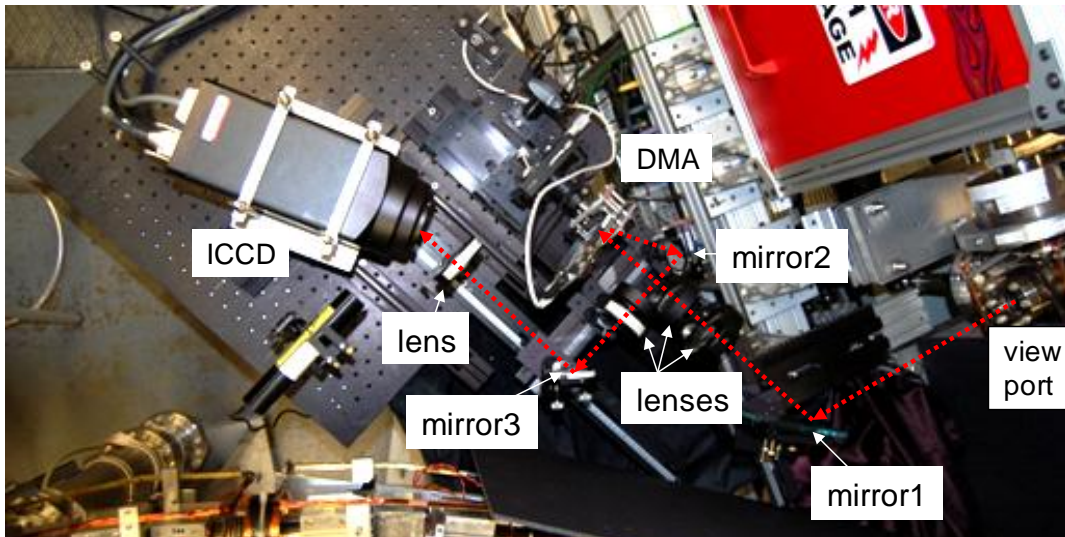
Figure 2.11: Experiment setup in UMER injection (IC1)
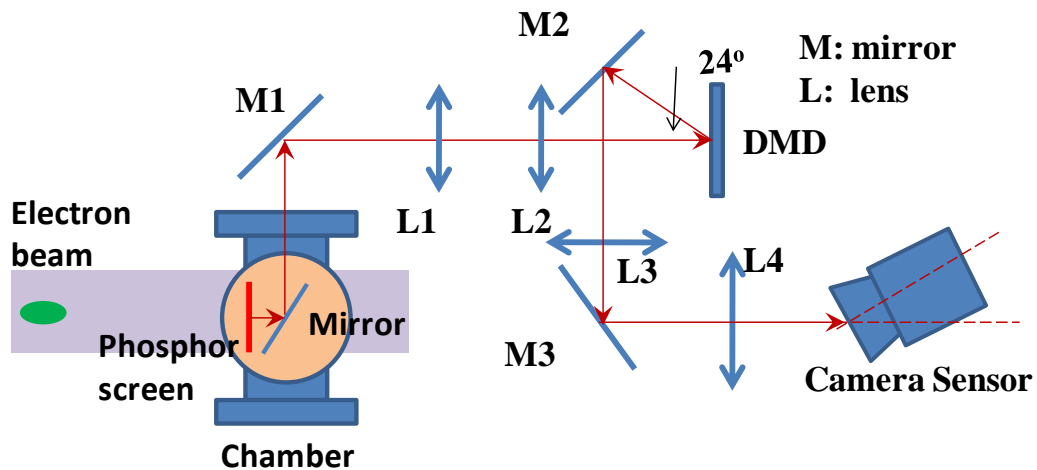
Figure 2.12: Layout of experiment setup in UMER ring (IC1)

In this design, comparing with the benchmark, additional mirrors (M1 and M2) are added to bend the light pathway because of the space limitation. The lenses

are chosen to satisfy the magnification as well as the space limitation. The magnification of each focusing channel is dependent on the size of the image source screen, DMD chip and CCD sensor. Notice that, the image source screen we use is a 31.75 mm diameter glass screen, coated with P-43 phosphor (Gd2O2S: Tb). This phosphor has an emission peaked in the green (545 nm) and a response time of 1.6 μs.

As a starting point in the design of the optics we tried to follow the benchmark design. The magnifications of the first and second optical channel should be approximately the same as the benchmark optics, which is 0.338 and 0.892. Based on these magnifications and taking actual space limitations into account, we use a simple ray tracking optical software [37] to get an optimal design solution. This software allow one to interactively adjust the focal lengths, radii, thicknesses and positions of all the lenses, as well as to determine how the extreme rays propagate, and the focal length and positions of lenses. The set of optical components for UMER experiment (IC1) and the calculation results from the optical code are listed in Table 2.3. The simulation of the light propagation is shown in Fig. 2.11.
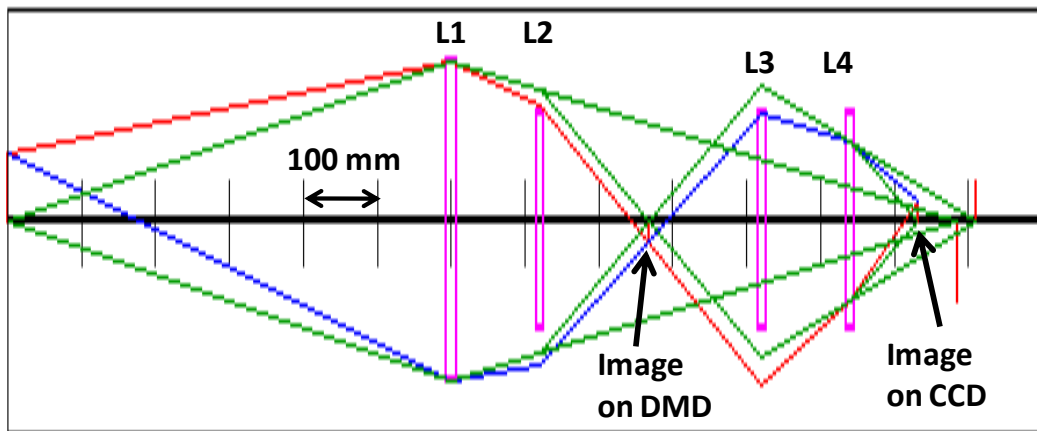
Figure 2.13: Optical simulation result of the light transport in IC1

Table 2.3: Optical component parameters for IC1

Component	Location*(mm)	Focus length(mm)	Radius(inch)	Other
L1	600	320	3	Achromat
L2	720	200	2	Achromats
DMD	868			
M2	928		2	Front surface
L3	1020	100	2	Achromats
M3	1100		2	Front surface
L4	1140	200	2	Achromats
CCD	1232			PIMAX2

*Location is the distance from the phosphor screen

The lenses used here are all achromats to minimize spherical and chromatic aberration, while the mirrors are all coated with aluminum on the front surface. Finally, by using the optics code, we obtain the magnification is 0.299 for the first channel, and 1.02 for the second channel. The actual magnification for the first channel is smaller than the benchmark design number (0.338) because of space limitations and limited choice of lenses which prevent us to match the screen diameter to the boundary of the DMD. This can be seen by comparing the calibration pictures Fig. (a) and (b), which shows that the screen occupies 337 pixels on the CCD sensor while the shortest side of DMD occupies 380 pixels, as is indicated by the red arrow on each figure.

From Fig. 2.14 (a) and (b), the size of the screen image on the DMD is 337/380*10.8 mm = 9.58 mm in the unit of the DMD. Therefore the magnification for the first channel from experimental calibration data is 9.58/31.75 = 0.302, which is close to the result from the optics simulation code (0.299). For the second channel,

we intentionally increased the magnification from 0.892 to 1.02 because we realized after our benchmark tests that the DMD frame could be off the range of CCD sensor, but the image of phosphor screen could still be imaged to the camera sensor. In fact it is desirable to make the screen image as large as possible to get better spatial resolution, as shown in Fig. 2.14 (b). The only constrain here is that we want to have a well-defined edge of DMD visible on the camera sensor in order to have a calibration for the generation of a mask on the DMD. This will be discussed later.

(a)   (b)
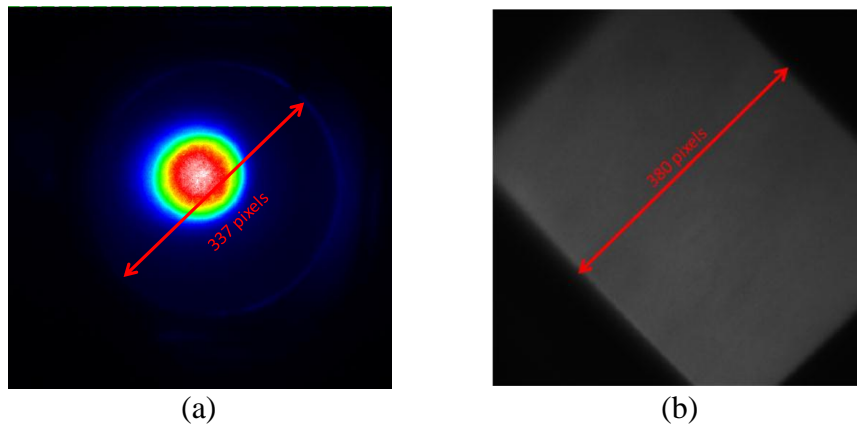
Figure 2.14: Calibration picture for IC1, (a) image of the phosphor screen (b) image of the DMD.

From Fig. 2.14 (b), the size of the DMD image on the CCD sensor is 380/512*15.8 mm = 11.7 mm. Thus the magnification for the second channel from experimental calibration data is 11.7/10.8=1.08, which is again close to the result from the optics simulation code (1.02). We list the experimental data for our magnification calculations in table 2.4.

In the experiment, all the lenses are set on rails to allow for adjustment. In addition all the optical components we have discussed are set on a moveable cart, so the entire optics system can be easily moved around the UMER ring. So the discussion in IC1 can be applied to any chamber in the UMER, e.g. the experimental setup at ring chamber, RC7.

Table 2.4: Calibration data for magnification calculation

Component	Real size	Image in CCD (Pixel)	Image in CCD (mm)	Image in DMD (mm)
CCD	15.8 mm	none	none	none
DMD	10.8 mm	380	11.7	none
Screen	31.75 mm	337	10.4	9.58

2.4 Algorithm for mask generation

Due to the 45° orientation of DMD and the difference in pixel number between DMD chip and CCD, in order to adaptively generate a mask for the beam core, a careful coordinates transforming and rescaling is necessary. The algorithm is shown schematically in Fig 2.12.
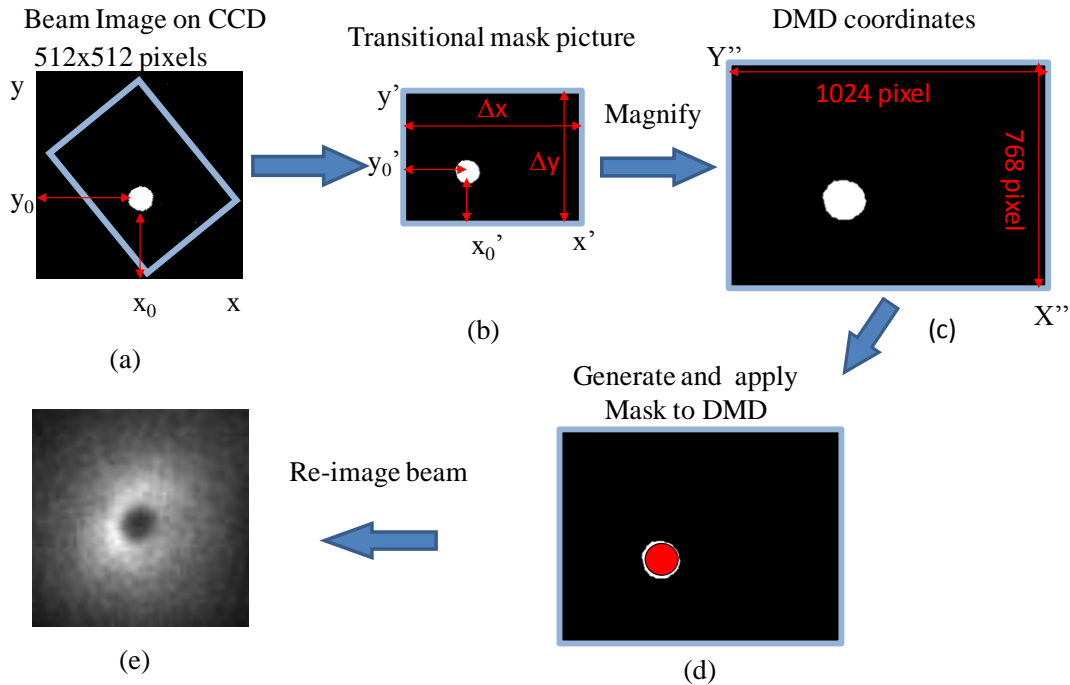
Figure 2.15: Schematic of mask generation algorithm

First we take a calibration picture to obtain the edge of DMD chip on the CCD, and thus determine the DMD chip size (Δx, Δy) as well as the equations

26

describing the edges of DMD chip in term of the CCD coordinates (x, y). This is the prerequisite step as shown in Fig. 2.12 (a).

Then, we generate a new 1-bit depth, $\Delta x \times \Delta y$ size, transitional picture with all pixels black (the pixel value is 0) as in Fig. 2.12 (b). For experiment, after we take beam picture, any point of interest (x_0, y_0), can then be transformed to transitional picture in terms of coordinates (x_0', y_0') by calculating the distance between the point and the edges of the DMD. We then choose selected discrete points on the beam image as a first step in generating a mask. There are many ways for defining the core. For example, we can use points in the 'core' of the beam as the selected points, by 1) specifying a particular geometric area (e.g. a circular disk) overlaid on the 'core' visually, or 2) setting an intensity threshold to define the 'core'.

Notice that, $(\Delta x, \Delta y)$ is still in the units of CCD pixels and is much smaller than the real size of DMD. Thus, for next step as shown in Fig. 2.12 (c) we linearly magnify the transitional picture by the ratio between its size $\Delta x \times \Delta y$ and DMD chip size, and generate the final 1-bit masking picture file, which can be read and used by the software supplied with the Discovery 1100 DMD to control the state of each micro-mirror pixel in the DMD. Here, in the 1-bit masking picture, black (0) or white (1) indicate "on" state (+12 ° state) or "off" state (-12 ° state) of each pixel. Following this algorithm we have described, a masking picture generation code based on MATLAB [38] which is presented in the Appendix C.

2.5 Chapter conclusion

In chapter 2, we described the concept of using a DMD in optics system, to observe beam halo, the optics we have developed for testing on the bench and show

27

how this system design can be applied to a real beam experimental setup. Based on the mechanics of the DMD described in chapter 2, we need employ several compensation techniques such as tilting the DMD and rotating the CCD camera to make the DMD useful as a spatial filter in a real optical system. These compensations methods affect the mask generation and the data acquisition, and so we have developed an algorithm for generating optical masks and a procedure for data acquisition which takes them into account (see the Appendix D).

Chapter 3: Experiment Results

As a new method in beam diagnostics, the validity of adaptive masking needs to be tested. In this chapter, we first discuss the methods we have employed to test the performance of the DMD imaging method including: 1) ability of the DMD to filter out the beam core (section 3.1); 2) the effect of the DMD on the quality of the beam image (section 3.2); 3) measurements of the dynamic range of the optics employing the DMD (section 3.3); and 4) the adaptivity of this method to changes in the beam core (section 3.4). After discussing the performance tests, we discuss the results of halo measurements using the DMD on the UMER beam in section 3.5.

3.1 Test of the Filtering Effect of the DMD

We first test the effectiveness of the DMD chip in filtering the beam image when the micro-mirrors are flipped from the "on" state to the "off" state. Here we follow the data collection procedure described in section 2.2.4, but set all the pixels from "on" to "off" states to mask everything on the DMD chip. Here, DMD control GUI software is used to read a 1-bit (black or white) 1024X768 picture and set all pixels of DMD chip to "on" or "off" states. We first take a UMER beam (here is 21 mA beam) profile with all DMD pixels to "on" state and the image is showed in Fig. 3.1(a), with peak intensity about 61500 counts. The maximum intensity level is 16 bits which is 65355; above this level the CCD pixels are saturated. Here the camera is set to integrate 180 beam pulse images. Next, for the same settings, we apply the white picture to the DMD, so all the pixels of DMD are "off". In order to compare with the previous one, we keep the integration setting to 180 frames resulting in the

image shown in Fig. 3.1 (b). Comparing these two images, in the beam region, the image with the white mask has an intensity level more than 10^3 less than the same region with the pixels "on". Fig. 3.1 (b) shows the beam region level (~50 counts) is almost at the noise level, which proves a good filtering effect of DMD chip. Notice that there are two visible lines (but with very small number counts ~10^2) seen in the image shown in Fig 3.1 (b). These lines are due to stray light scattered from the edges of DMD chip. Therefore, we conclude that the DMD is effective in masking as a filter.
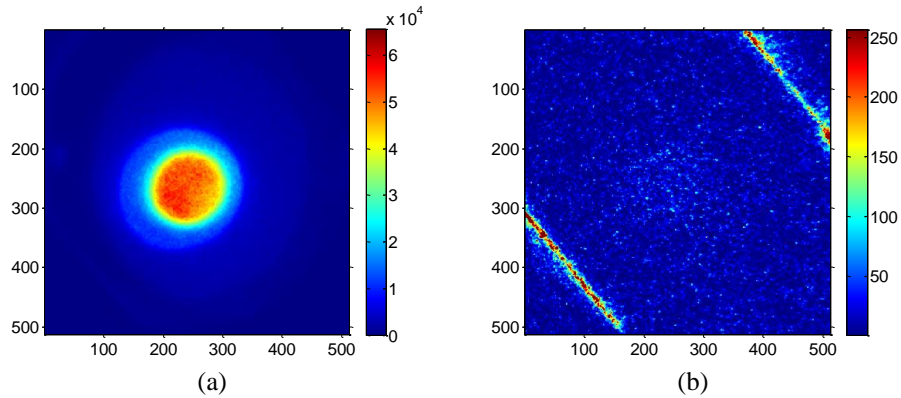
Figure 3.1: (a) Image with all DMD pixels set to +120; (b) image with all pixels set to -120; vertical and horizontal coordinates are given in terms of CCD pixels

3.2 Effect of diffraction and Scheimpflug compensation on image quality

The effect on the quality of the image reflected from the DMD micro-mirrors is an important issue. As discussed previously, because of the segmentation of the micro-mirrors, the DMD chip behaves like a 2D grating, and so diffraction may be a potential problem. In addition, we use the Scheimpflug principle to compensate for the tilting of the first image plane (at the DMD), as discussed in section 2.1, due to the 12-degree tilt of the micro-mirrors. Thus, we also want to test the effectiveness of

this compensation. Therefore, as a second step, we did an experiment to test whether the DMD affects the final image quality.

Three different conditions are used to test the image quality as showed in Fig. 3.2: (a) is in the normal condition where all the DMD chip pixels are set to the "on" state and Scheimflug compensation is used (as done in Fig.3.1); b) is "float" state where all the DMD pixels are in the floating state and no compensation is used; and c) the DMD is replaced by a simple mirror and no compensation is used.

Fig. 3.2 shows the beam images taken for each of these cases. Note that the optics must be slightly adjusted between configurations. This causes slight differences in the magnification and number of peak counts for each case. Therefore, we have normalized the intensities by the peak values in each image in order to concentrate on differences in the beam profile. No major differences are observed. We conclude that diffraction and scattering by the DMD mirrors has little if any effect on the quality of the beam images and that proper compensation produces a high quality image as well.

(a)   (b)   (c)
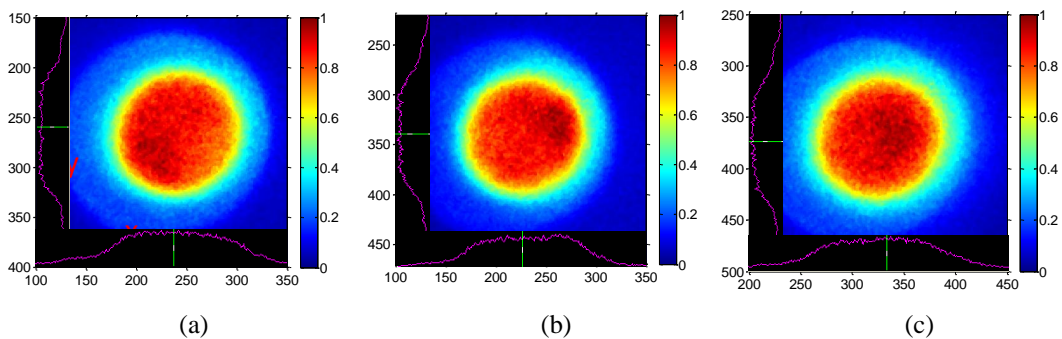
Figure 3.2: Comparison of beam images with: (a) all DMD pixels set to '+' and Scheimflug compensation; (b) all DMD pixels floating and no compensation; (c) simple mirror and no compensation.

31

3.3 Measurement of the Dynamic Range of the DMD Optical System

In order to determine the dynamic range of the entire optical system we observed an intense beam (I=21mA) focused to a 2.85 mm diameter spot on the phosphor screen, the minimum achievable size with our solenoid focusing magnet (the beam is small enough that this spot coincides with the centroid within experimental error). We then generated a number of circular masks with different radii but a common origin, i.e. the position of the peak intensity of the beam observed without a mask.
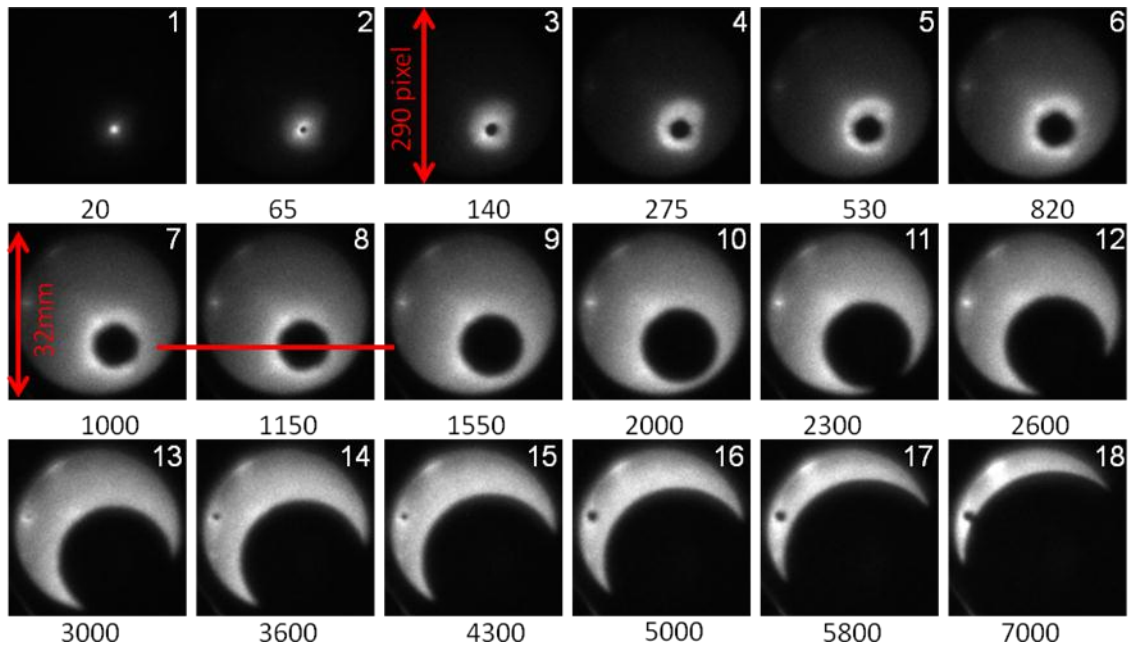
Figure 3.3: Images of the focused beam with the DMD set to concentric circular mask of successively larger radii; number below image denotes the number of frame integrations on the ICCD camera

For each mask, we selected the appropriate number of frames (the number is written underneath each photo in Fig. 3.3) on our ICCD camera necessary to bring the peak intensity in the image to near the saturation level of the camera. Note the small highlights visible in the upper left hand part of pictures in the second row. These are

due to scattering of the phosphor light from the metal edge of the screen. We added a second small mask to block out these highlights, which is seen as black dots on the lower images of Fig. 3.3.
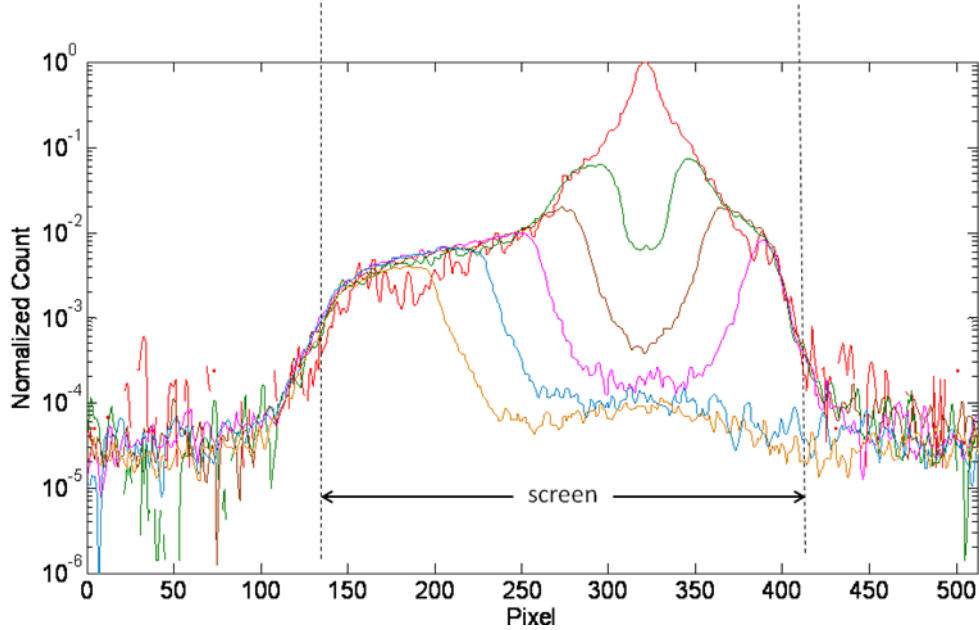
Figure 3.4: Normalized horizontal scans of selected beam images presented in Fig. 3.3

To obtain a background image, we turned the beam off and integrated for the same number of frames used to obtain the beam image. Background subtracted images are shown in Fig. 3.3; the number below each picture is the number of frames used to obtain that particular image. By taking the horizontal line's scans of all beam profiles (note for reference the horizontal red line in Fig. 3.3) and normalizing by the number of frames taken for each image, we can present the results as a series of normalized plots as shown in Fig. 3.4. The scans in the Fig. 3.4 correspond to number 1, 4, 7, 10, and 13 (this number is on upper right of each photo) of the pictures in Fig. 3.3. Note that the intensity fluctuations in tails of the beam profiles get smaller as more integration is applied. Moreover, the noise level outside the screen decreases to

33

~10^{-5}. Using the data presented in Fig. 3.3, and Fig. 3.4, we can reconstruct the 2D beam image (normalized) as shown in Fig. 3.5.
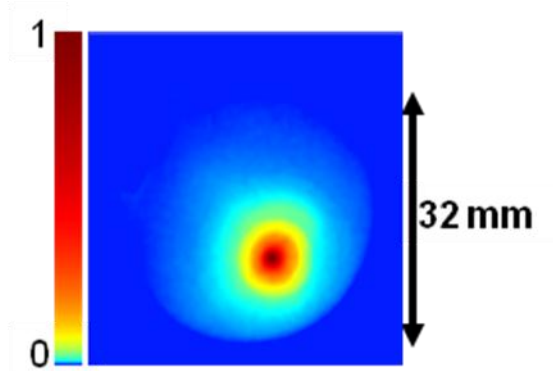
Figure 3.5: Reconstructed focused beam image using a logarithmic intensity scale

3.4 Halo imaging with an adaptive mask

The key advantage of the DMD method is the ability to adaptively mask the beam core. Therefore, we did a halo imaging experiment in IC1 to test the effectiveness of adaptive masking. Previous study [16] shows that, changing the bias voltage in the gun will artificially enhance halo.

Fig. 3.6 (a) shows a greyscale image of the 21 mA beam with halo when bias voltage is 50 V (the default bias voltage is 30V). Note that neither the core nor the halo distributions are axisymmetric. However, by setting a threshold condition (e.g. 10^4 counts), we used the DMD to create an optical mask which conforms or adapts to and selectively blocks out the 'core', i.e. all pixels in the beam image with intensity levels greater than the threshold. As described above, we then increased the number of integration frames, bringing the peak intensity of the halo close to saturation, to better view the halo distribution. The ratio of the number of frames integrated with the DMD mask (180) to those taken without the mask (900) is five, which effectively increases the dynamic range of the measurement.
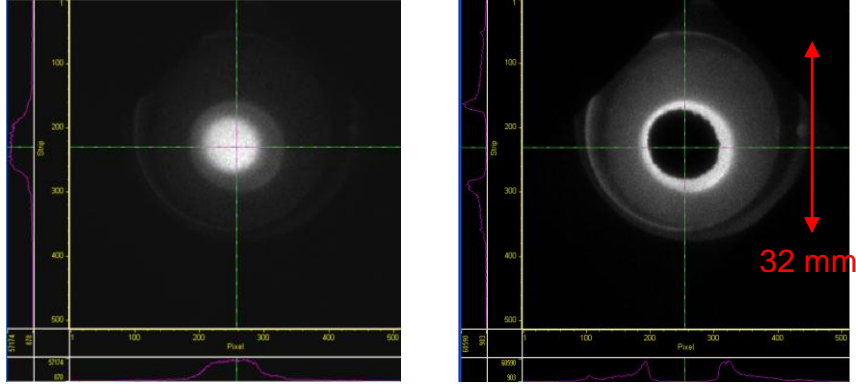
Figure 3.6: (a) Beam image with core and halo; (b) image of the halo after applying adaptive threshold mask with intensity level of 10^4 counts.

By lowering the threshold level and increasing the integration time, similar to what was done with the circular masks (see Fig. 3.3), we can view the tail of the halo distribution, up to the limit of the screen size, with a further increase in dynamic range. Therefore, we did a dynamic range measurement using an adaptive mask. We used the 21 mA beam with bias voltage 50 V. We show the results in Fig. 3.7, where the number underneath each pictures is the integration number used to obtain that particular image and the number above is the intensity threshold according to the picture with lower index (upper right). By taking the horizontal line's scans of all beam profiles again (note for reference the horizontal red line in Fig. 3.7) and normalizing by the number of frames taken for each image, we can present the results as a series of normalized plots as shown in Fig. 3.8. Note that this threshold mask method measures the transverse beam structure very well: a flat beam core and an intense halo with a Gaussian tail. The pictures also show the centroids of beam core and halo do not coincides. The horizontal scans show a good dynamic range about 10^{-4} (limited by the noise level in the scan). Using the data presented in Fig. 3.7, and Fig. 3.8, we can reconstruct the 2D beam image (normalized) as shown in Fig. 3.9.
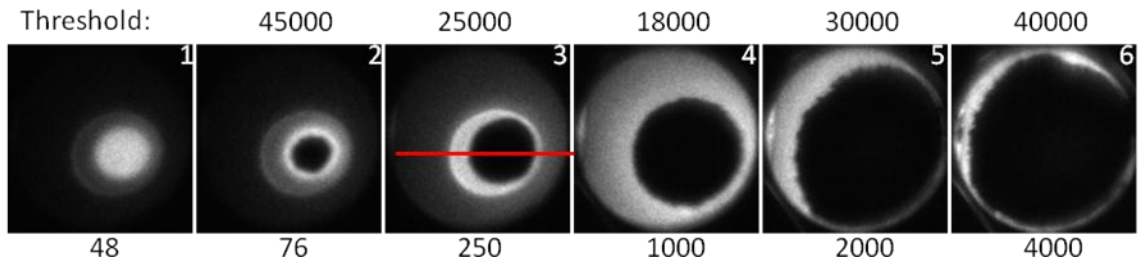
Figure 3.7: Images of the stu beam with the DMD set to adaptive mask of successively intensity threshold; number below image denotes the number of frame integrations on the ICCD camera
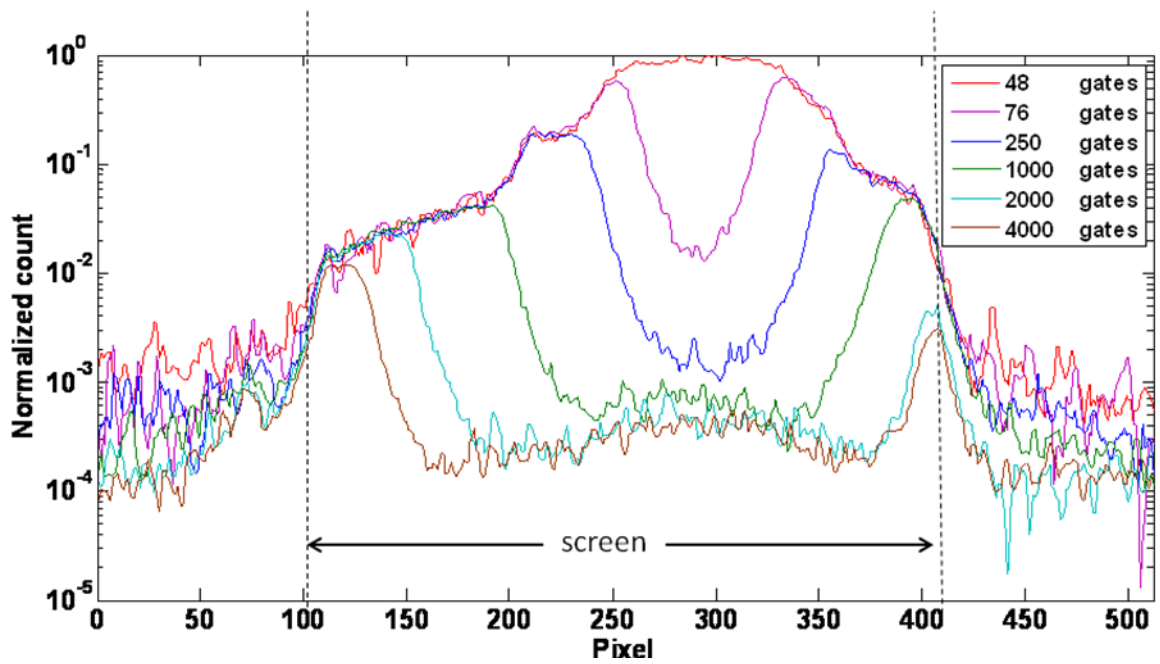
Figure 3.8: Normalized horizontal scans of all beam images presented in Fig. 3.3
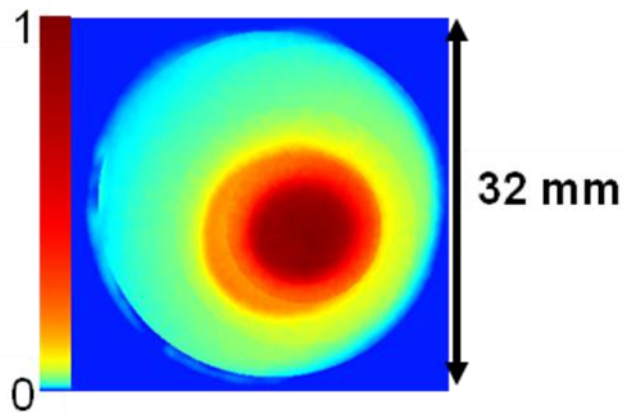
Figure 3.9: Reconstructed beam image with halo using a logarithmic intensity scale

3.5 Beam halo variation caused by quadrupole error

Following the halo imaging strategy described in section 3.4, we redid the experiment in the UMER ring chamber (RC7) by varying the focusing strength of quadrupole (QR2), which has the effect of changing beam core shape as well as the halo distribution. As we change the quadrupole strength, the beam become mismatched and the resulting mismatch oscillation leads to a different beam shape in each of the chamber. In addition, the mismatch results in the formation and transformation of a halo. We have imaged both the beam and halo at ring chamber (RC7), which is about one third of ring circumference downstream of QR2 and show the results about 21 mA beam and 6 mA beam in Fig. 3.10 and Fig. 3.11, respectively.

Figure 3.10 Comparing core and halo with changing quadrupole strength
(a) Unmasked beam picture; (b) masked beam picture

Fig. 3.10 shows a group of beam images taken with the 21 mA aperture, where the numbers in the lower left is the integration frames and the number between row (a) and (b) is the threshold intensity level to generate the mask. We decrease the original quadrupole current strength (I_Q) by 12.4% and 28.8% to see the changes in both the beam core and the halo. Here, a decrease in the quadrupole current will result in a linear drop in the quadrupole magnetic field and thus increase the focus length of the quadrupole. Row (a) in Fig. 3.10 shows photos of the beams for all settings, which indicates that the core gradually enlarges in the x direction and shrinks in y direction, becoming elliptical. Row (b) shows the same beam after applying a threshold mask at the level indicate in the middle. This experiment verifies a good adaptability of this masking method in the circumstance of beam core variation. We also see that decreasing the quadrupole current strength will also affect the halo distribution. Notice that more particles are driven out of the core, as shown in Fig. 3.10, when the size of high intensity region becomes larger outside the beam core. Because the beam size is large, some particles in the halo are already off the screen, which means they may collide with the pipe and become lost.

In order to see the full extent of the halo, a much smaller beam with 6 mA current (usually the radius is 0.875 mm as indicated in Table 2.2) is used here. We again decrease the original quadrupole current strength (I_Q) by 17.1%, 33.7% and 50.3% to see beam core and halo variation. Fig. 3.11 shows the results. Comparing the pictures in Row (a), we see the beam centroid gradually moves toward the negative y-direction. This may be the result of quadrupole misalignment with respect to the center of beam pipe or beam misalignment. By decreasing the quadrupole

current, the beam shrinks in the x direction and expends in the y direction. In Row (b), as the quadrupole current decrease, particles escape from the beam core and appear to rotate in the halo region. The typical halo size is 2 or 3 times greater than that of the beam core.
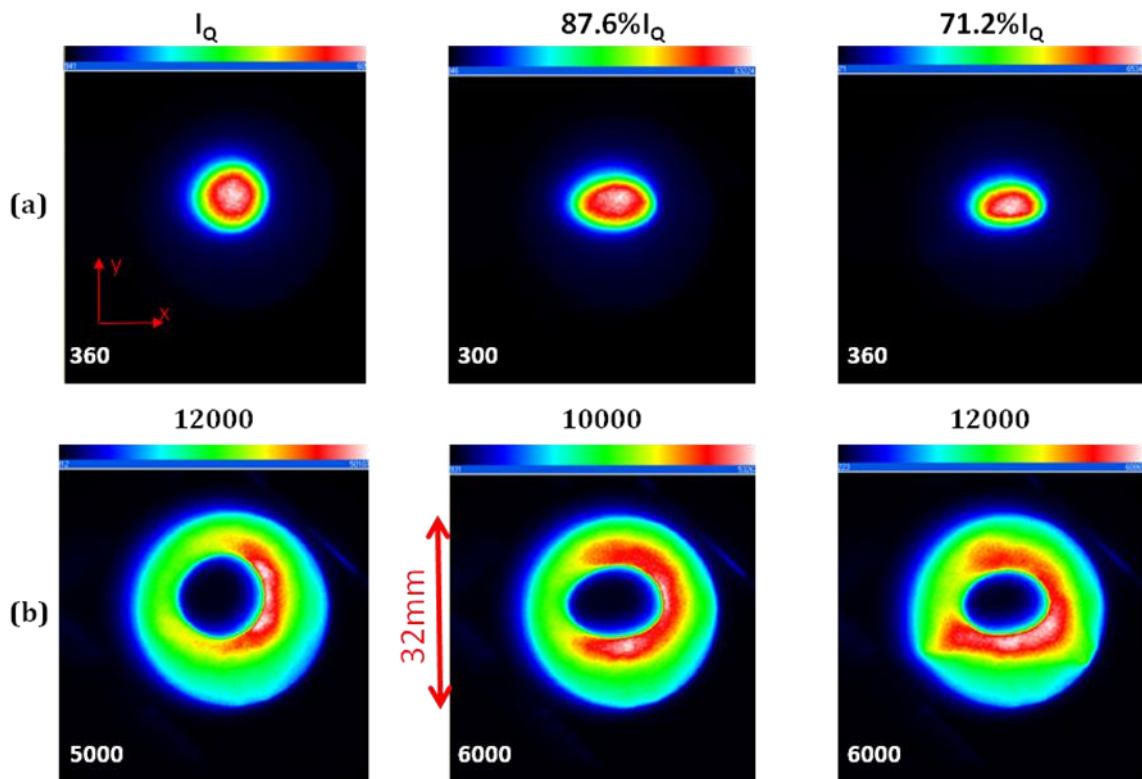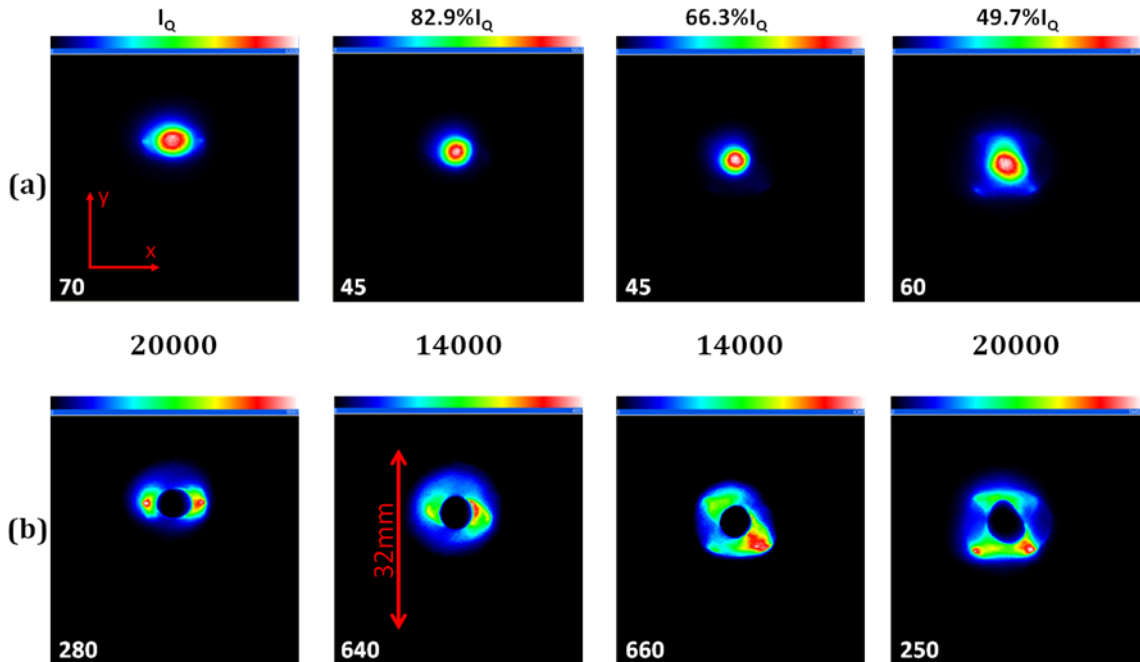

Figure 3.11 Comparing core and halo with changing quadrupole strength
(a) Unmasked beam picture; (b) masked beam picture

3.6 Chapter conclusion

In Chapter 3, we apply the DMD masking method to image the halo of a real beam at UMER. We show a good filtering ability of the DMD, and demonstrate that the quality of the beam image is little affected by the diffraction effects due to the DMD itself and the Scheimpflug compensation method required to obtain an image of the beam with the DMD in the optical path. These two steps insure the reliability of the results from this method. In addition, we measure dynamic range of ~ 10^5 with this method using a tightly focused UMER electron beam with a simple phosphor

screen. This matches earlier measurements [33] taken using the DMD with laser only. We also show the capability of this method to measure beam halo using a threshold mask. The dynamic range measured is limited by the size of our imaging screen, the highest beam intensity achievable, the efficiency of the phosphor, the ratio of the minimum beam size to the screen size, and the scattered light as well as background light level. These limitations may be exceeded at other machines which have a higher intensity beam and/or with improved optics which limit diffraction due to the lenses and the mask, e.g. a Lyot stop such as used in coronagraphy. Moreover, we use the DMD masking method to image the halo of real electron produced at UMER. We show the flexibility of this method in masking the beam core with different shapes, and discover some halo formation and propagation phenomena according to bias voltage in the gun or quadrupole mismatch in the ring.

Chapter 4: Conclusion

4.1 Summary

The goal of this thesis to develop a new imaging method to measure beam halo. As discussed in Chapter 1, measurements of beam halo are essential to optimize accelerator performance and reduce effects detrimental to the operation of all accelerators. We have mentioned several mechanisms of beam halo formation We have addressed the importance of dynamic range for the methods in halo measurement and also briefly reviewed several methods for measuring halo. A new i method to image beam halo has been developed and tested using a DMD.

In Chapter 2, we have described the operation of benchmark optics using DMD and explained the imaging process. Several techniques have been applied to optical system in order to compensate for problems introduced by the properties of the DMD itself, which facilitate its use in a real beam diagnostics environment. We have developed and test a flexible imaging system for use on UMER which can be applied to any accelerator and the data collection hardware and software to make such a system easy to operate. In particular we have developed the necessary mask generation algorithms and computer codes and data collection procedures.

In Chapter 3, the effectiveness of this method has been proved through the filtering and image quality tests. We have shown effects of diffraction and scattering due to the DMA on beam images are minimal, as well as shown the adaptivity of this method to changes in the beam shape. The dynamic range of the entire optical system has been measured using a real electron beam and shown to be ~10^5, which matches t

previous experiments using DMD and a laser [33]. We have done two specific imaging experiments using 21 mA and 6 mA electron beams at UMER, and observed phenomena of halo formation and evolution.

4.2 Future Plans

As discussed in Chapter 2, UMER is a test bed to show the effectiveness of this method. Some features of UMER and the imaging screen used in our measurements, such as the highest beam intensity achievable, the efficiency of the phosphor, the ratio of the beam to the screen size, scattered light and background, limited our measured dynamic range, and thus the observed range of the halo. Potential improvements can be done such as introducing additional components to the optics, e.g. Lyot stop to further eliminate the diffraction and polarizer to remove scattering light from background or transporting channel, using other beam based emissions, e.g. YAG screen, synchrotron radiation, OTR (optical transition radiation) or optical edge radiation. Otherwise, with proper modification and improvement of benchmark optics, this method can be applied to any higher energy accelerator as well.

Using this existing system, future experiments can done on UMER to test theories of beam halo formation due to parametric resonance, quadrupole rotation error,etc. We can also observe longitudinal halo phenomena by using our optical system and gated intensifier with a fast (3ns) phosphor screen available on UMER. We also plan to apply the technology presented in this thesis to design a similar setup at the Free Electron Laser Facility at Jefferson Laboratory which will use optical synchrotron light as the source.

Appendix A: optical alignment procedure

This appendix contains the alignment procedure for the optical system described in section 2.1, benchmark test. In general it can also be used to alignment the experimental system used in UMER or any other machines. In consideration of the real experiments, we cannot align the whole optics from the very beginning because of the space limitation around the beam machine. A laser and an extra mirror, combined with the beam splitter are used here to align all the optical components from the backward. The specific procedure is listed as follow:

1) Adjust all optical component central to the same height;

2) Take out beam splitter and all lenses;

3) Shoot laser directly into the mirror right in front and adjust that mirror to reflect the laser back;

4) Put in the beam splitter to split the laser and rotate it until laser hit mirror 1;

5) Adjust the mirror until laser hits the center of DMD;

6) Turn on DMD and set all pixel to the "on" state and rotate it 45^0 about the optics line;

7) Swing the DMD about vertical line to guide the laser to the center of target;

8) Put in lenses one by one and repeat step 5 and 7 until the laser is centered on the target.

Appendix B: Scheimpflug principle

This appendix contains the derivation of Equation 2.3. As discussed in [34], the plane of DMD, effective lens and the CCD sensor will intercept in one point (also shown in Fig. B.1).
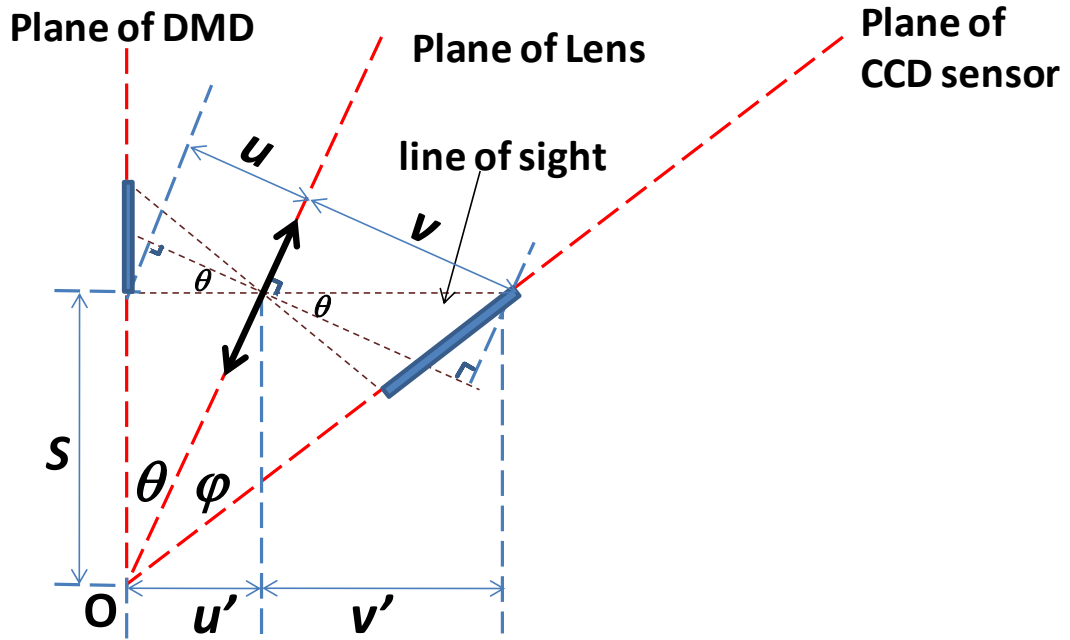
Figure B.1: Illustration of Scheimpflug principle

From Fig. B.1,

$$S = \frac{u'}{\tan\theta} = \frac{u'+v'}{\tan(\theta+\varphi)} \tag{B.1}$$

Where u' and v' are the object and image distances along the line of sight, and S is the distance from the line of sight to the Scheimpflug intersection at point O, θ is the DMD configuration angle according to the plane of effective lens shown in Fig. 2.4 and Fig. 2.5, and φ is the angles of the plane of the CCD sensor with respect to the plane of the effective lens.

Also from Fig. B.1,

$$u = u'\cos\theta$$
$$v = v'\cos\theta \tag{B.2}$$

Where u and v are the projected object and image distances along the line perpendicular to the plane of lens and from the equation of magnification as shown in Fig. B.1,

$$m = \frac{v}{u} \tag{B.3}$$

Combining these three equations, we can get the relationship between φ and θ expressed in terms of the magnification m of the object in the line of sight:

$$\varphi = \arctan(\frac{m+1}{m}\tan\theta) - \theta \tag{B.4}$$

Which is the equation expressed as Eqn. 2.2.

Appendix C: Mask generation code

This Appendix contains the MATLAB code used in the thesis to generate mask. The algorithm is discussed in section 2.2.3. As suggested in section 2.2.4, some part of the code need to be updated every time in case the location or magnification is changed by intention or accident. Below are the details:

```matlab
function MaskGeneration(filename)
%Function is used to generate mask picture which can be applied in DMD GUI
software
%Created by Hao Zhang
%filename is the original beam profile image which the mask base on

%-----------------Define location of DMD in CCD---------------------------
y = [507,370,204,56,34,237,404,502]; %DMD edge in the coordinate of CCD from
x = [191,14,7,123,217,496,503,428];   %calibration need to update every time before
                                       %generate new mask

A=[0,0]; B=A; C=A;  %line parameter of two edge(two point define a line)
for n=1:2
   A(n) = (y(2*n)-y(2*n-1))/(x(2*n)-x(2*n-1));
   B(n) = -1;
   C(n) = -(y(2*n)-y(2*n-1))/(x(2*n)-x(2*n-1))*x(2*n-1)+y(2*n-1);
End

%The length and width of the DMA in units of CCD pixel
Lx = ceil(abs(A(2)*x(8)+B(2)*y(8)+C(2))/sqrt(A(2)^2+B(2)^2));
Ly = ceil(abs(A(1)*x(5)+B(1)*y(5)+C(1))/sqrt(A(1)^2+B(1)^2));
%--------------------------------------------------------------------------------------

%--------------------------mask generation------------------------------------------
Pic = imread(filename,'tif');  %read file
threshold = 10000;            %threshold level
Core = find(Pic>threshold); %core region
[a,b] = size(Pic);
NewPic = zero(a,b,'double'); %Mask picture in unit of CCD
NewPic(Core) = 1;             %set Core region to 1, others zero

dmd=ones(Ly,Lx,'double'); % Demagnified DMD in unit of CCD pixel, all "on"
for i=1:512
   for j=1:512
      if NewPic(i,j) == 1     %find the core point
```

```matlab
        ix = ceil(abs(A(2)*i+B(2)*j+C(2))/sqrt(A(2)^2+B(2)^2));%Screen
Coordinates X
        iy = ceil(abs(A(1)*i+B(1)*j+C(1))/sqrt(A(1)^2+B(1)^2));%Screen
Coordinates Y
        dmd(iy,ix) = 0; %the point we interested set to Black (which will not  reflect
to
                        %the camera)
      end
   end
end

dmd = medfilt2(dmd); % fill the conjunction points inside the core
DMD = imresize(dmd,[768,1024]); %enlarge  the reduced DMD picture to real size
clear dmd;
DMD = medfilt2(DMD,[4,4]); % avoid sharp edge

for j=1:768
   for i=1:1024
      Mask(j,1025-i) = DMD(j,i);  %mirror image
   end
end
%----------------------------------------------------------------------------------------------
----

Maskname = ['mask.bmp'];
imwrite (Mask, Maskname, 'bmp');  %save
```

Appendix D: Data collection procedure

This appendix includes the data collection procedure for experiments.

1) Using the system describe in this system, a final adjustment needs to be done before the experiment including adjusting the alignment, correcting focus and magnification.

2) A pre-experimental calibration of the DMD needs to be done to update the new position of DMD in terms of the coordinates of the CCD. For this step, we apply an all-"on" picture to DMD through the GUI software, illuminate the DMD by a uniform light source, use camera's shutter mode to acquire a picture of the DMD, record the two point position of each edge of DMD in the picture, and update them in the MATLAB code to renew the code for mask generation.

3) A real measurement begins. We initially take a picture of the whole beam using the camera's gate mode. To make sure the synchronicity between the beam arrival and opening of the shutter, an external trigger ahead of the beam arrival time at the phosphor screen is plugged into the camera programmable timing generator. By adjusting the delay in the camera control software, we can make sure the arrival time at the screen is synchronous to opening of the shutter. Here, because the beam duration time is 100 ns, we set the gate width of the camera's gate a little bigger, for example 160 ns. If the beam is weak, we need to acquire several gated images prior to readout, in order to allow the peak intensity of beam profile to approach the saturation of CCD bits limitation (2^{16} counts).

4) Run the MATLAB code to generate a new 1-bit mask picture either by prescribing a certain shape (e.g. a circular disk) or a given intensity threshold (with

beam core value 0, which means "off" to DMD pixel, while others value 1, which means "on" to DMD pixel).

5) Run the DMD GUI software again to apply the new mask to the DMD. Finally, retake the beam profile picture. Here, since the high intensity part is blocked out, we need more integrate frames to get the peak intensity of the rest beam profile to approach the saturation of the CCD. This process allows us to utilize the full dynamic range of the CCD which is defined as the ratio of the full electron well capacity of a divided by the total noise level.

Bibliography

[1]   R. R. Wilson. The Tevatron. *Phys. Today*, 10:23–30, 1977.

[2]   P. Emma. The Stanford Linear Collider. *Proc. of PAC95*, vol.1, 1995: 609 – 610.

[3]   L. Evans. The Large Hadron Collider. *New J. Phys*, 9:335, 2007.

[4]   J. N. Galayda. The advanced photon source. *Proc. of PAC95*, vol. 1, 1995.

[5]   J. B. Murphy, et al. NSLS II: The future of the NSLS. *Proc. of PAC05*: 3345–3347

[6]   P. G. O'Shea and H. P. Freund. Free-Electron Lasers: Status and Applications. *Science*, Vol. 292, No. 5523, Jun. 8, 2001: 1853-1858

[7]   R. Tatchyn, et al. Research and development toward a 4.5-1.5 Å Linac Coherent Light Source (LCLS) at SLAC. *Nuclear Instruments and Methods in Physics Research Section A*, 375, 1996.

[8]   A. S. Schwarz. The European X-ray free electron laser project at DESY. *Proc. of the 2004 FEL Conference*: 85-89.

[9]   G. S. Bauer. Physics and technology of spallation neutron sources. *Nuclear Instruments and Methods in Physics Research Section A: Accelerators, Spectrometers,Detectors and Associated Equipment*, 463(3):505–543, 2001.

[10] R. Bock. Heavy Ion Fusion. *IEEE Transactions on Nuclear Science*, Vol. NS-30, No. 4, August 1983.

[11] Martin Reiser. *Theory and Design of Charged Particle Beams*. Wiley-VCH, 2nd edition, 2008.

[12] A. V. Fedotov. Beam halo formation in high-intensity beams. *Nuclear Instruments and Methods in Physics Research A*, 557 (2006): 216–219.

[13] D. Jeon, et al. Formation and mitigation of halo particles in the Spallation Neutron Source linac. *Phys. Rev. ST Accel. Beams*, vol. 5, 094201 (2002)

[14] Y. Shimosaki and K. Takayama. Halo formation at early stage of injection in high-intensity hadron rings. *Phys. Rev. E* 68, 036503 (2003).

[15] I. Haber, et al. Collective space-charge phenomena in the source region. *Nuclear Instruments and Methods in Physics Research A* 519 (2004) 396–404

[16] R. L. Gluckstern. Analytic model for halo formation in high current ion linacs. *Phys. Rev. Lett.*, 73(9):1247–1250, 1994.

[17] T. P. Wangler, et al. Particle-core model for transverse dynamics of beam halo. *Phys. Rev. ST Accel. Beams*, 1(8):084201, 1998.

[18] J. Qiang, et al. Space-charge driven emittance growth in a 3d mismatched anisotropic beam. *Phys. Rev. Lett.*, 92(17):174801, Apr. 2004.

[19] M. Ikegami. Particle-core analysis of mismatched beams in a periodic focusing channel. *Physical Review E*, 59(2):2330–2338, 1998.

[20] R. A. Kishek, et al. Beam Halo from Quadrupole Rotation Errors. *Beam-Halo Dynamics, Diagnostics, and Collimation*, vol. 693, pp. 89–92, 2003.

[21] C. F. Papadopoulos. Beam halo creation and propagation in the University of Maryland Electron Ring. PhD thesis, University of Maryland, College Park, 2009.

[22] T. Shea and P. Cameron. Halo Diagnostics Overview. *Beam-Halo Dynamics, Diagnostics, and Collimation*, vol. 693, pp. 9-13, 2003.

[23] B. Bouchet, et al. Wire-Scanners at LEP. *Proc. of the 1991 IEEE Part. Accel. Conf.*, San Francisco, 6-9 May 1991

[24] C. K. Allen, et al. Beam-halo measurements in high-current proton beams. *Phys. Rev. Lett.*, 89(21):214802, 2002.

[25] J. D. Gilpatrick. Wide Dynamic-Range Beam-Profile Instrumentation for a Beam-Halo Measurement: Description and Operation. *Beam-Halo Dynamics, Diagnostics, and Collimation*, vol. 693, pp. 122-125, 2003.

[26] P. Cameron, et al. The RHIC Ionization Beam Profile Monitor. *Proc. of PAC99*: 2114-2116, 1999

[27] R. Connolly, et al. Residual-Gas-Ionization Beam Profile Monitors in RHIC. *Proc. Of BIW10*, 2010

[28] G. Haouat, et al. Experimental study of the E.L.S.A. electron-beam halo. *AIP Conf. Proc.* Vol. 333, pp. 245-251, 1995

[29] C. P. Welsch, et al. A Beam Halo Monitor Based on Adaptive Optics. *Proceedings of the SPIE*, Volume 6616, pp. 66160M (2007).

[30] T. Mitsuhashi. Design and Constriction of Coronagraph for Observation of Beam Halo. *Proceedings of EPAC 2004*, Lucerne, Switzerland.

[31] Texas Instruments Inc. DMD Discovery 1100 Controller Board and Starter Kit, 2005.

[32] J. Egberts. Investigations on transverse beam profilemeasurements with high dynamic range. Master thesis. University of Heidelberg, Heidelberg, 2009.

[33] P.G. O'Shea et al, The University of Maryland Electron Ring (UMER). *NIM A* 464, 646-652 (2001).

[34] T. Scheimflug, "Improved Method and Apparatus for the Systematic Alteration or Distortion of Plane Pictures and Images by Means of Lenses and Mirrors for

Photography and for other purposes", GB Patent No. 1196. issued 12 May 1904; see also http://www.trenholm.org/hmmerk/#SR.

[35] R.A. Kishek, et al. The University of Maryland Electron Ring (UMER) enters a new regime of high-tune-shift rings. Proc. of PAC 07 p. 820 (2007).

[36] UMER Beam Parameters, UMER report, 2010, also see http://www.umer.umd.edu

[37] A. Shkvarunets. Optical code for imaging.

[38] Matlab, by The MathWorks, Inc.

[39] H. M. Marklinger, *Focusing the View Camera*. Bedford, Nova Scotia: Seaboard Printing Limited. 1996.